JGR Solid Earth

RESEARCH ARTICLE
10.1029/2024JB030910

Coupled Paleomagnetism and $^{40}Ar/^{39}Ar$ Dating of Latera Ignimbrites (Vulsini Volcanic District, Italy) Unravel Processes Associated to Piston-Collapse Calderas

Arianna Beatrice Malaguti[1,2], Stéphane Scaillet[3], Marco Pistolesi[4], Mauro Rosi[4], Fabio Speranza[2], and Alberto Renzulli[5]

[1]Istituto Nazionale di Geofisica e Vulcanologia, Osservatorio Etneo-Sezione di Catania, Catania, Italy, [2]Istituto Nazionale di Geofisica e Vulcanologia, Rome, Italy, [3]Université Orléans, CNRS, BRGM, Institut des Sciences de la Terre d'Orléans (ISTO), UMR 7327, Orléans, France, [4]Dipartimento di Scienze della Terra, Università di Pisa, Pisa, Italy, [5]Dipartimento di Scienze Pure e Applicate, Università degli Studi di Urbino Carlo Bo, Urbino, Italy

Abstract Correlation of ignimbrite units at polygenic calderas is mandatory for the reconstruction of caldera-forming events and proper identification of their eruption dynamics. However, ignimbrites erupted at different times from the same caldera can display similarities in composition and lithology that can hamper proper correlation of outcrops across the caldera structure. Here, high-resolution paleomagnetic and $^{40}Ar/^{39}Ar$ data are used along with stratigraphic evidence to address and resolve the relationships between two ignimbrites associated with the Latera caldera (Grotte di Castro and Onano Formations, Vulsini Volcanic District, Central Italy). These were characterized at 32 paleomagnetic sites and eleven $^{40}Ar/^{39}Ar$ sampling sites encompassing proximal and distal facies. Overall, the paleomagnetic directions of the two ignimbrites are statistically indistinguishable whereas single-grain $^{40}Ar/^{39}Ar$ ages of sanidine and leucite crystals show systematic preservation of pre-eruptive ages with sectorial variations closely controlled by eruption dynamics, yet with a neatly defined common juvenile (syn-eruptive) age at 205 ka. The data show that the two ignimbrites are the product of a single event, here renamed the "Grotte di Castro-Onano" eruption, representing the largest and latest caldera-forming stage of the Latera system. The sectorial preservation of pre-eruptive $^{40}Ar/^{39}Ar$ ages across the depositional sequence is interpreted to reflect the extraction processes with selective (re)mobilization of magma batches associated to piston collapse dynamics. Coupling paleomagnetism with $^{40}Ar/^{39}Ar$ dating is shown to be a key step in such cases for successful resolution of individual caldera-forming events at the millennial scale.

Plain Language Summary Ignimbrites are highly explosive volcanic products typically spread over wide areas around calderas. Many calderas are polygenic implying that they formed as a result of repeated ignimbrite events whose mineralogical and geochemical features can be similar. In addition, ignimbrites can also display internal facies variations and sectorial zoning due to complex emplacement mechanisms. Collectively, these factors can hamper correlation and clearcut identification of key eruptions in the sequence. Here, we report new paleomagnetic and $^{40}Ar/^{39}Ar$ data sets coupled with stratigraphic evidence to address the possible correlation among two major ignimbrites that were previously mapped as separate eruptions of the Latera caldera (Vulsini Volcanic District, Central Italy). The new $^{40}Ar/^{39}Ar$ data and paleomagnetic correlations allow merging the Grotte di Castro and Onano formations into a single eruptive event, renamed "Grotte di Castro-Onano," dated at 205 ka. The widespread occurrence of pre-eruptive crystals older than 205 ka in juvenile (syn-eruptive) facies sheds light on emplacement dynamics and magma extraction processes associated with caldera forming events worldwide.

Key Points:

- Similar $^{40}Ar/^{39}Ar$ ages and paleomagnetic data suggest Grotte di Castro and Onano Fms. form a single compound eruptive unit
- Intra-ignimbrite $^{40}Ar/^{39}Ar$ variations indicate these occur as the result of selective extraction dynamics from a compound magma chamber
- Sanidine and leucite $^{40}Ar/^{39}Ar$ ages suggest cold storage and a stable thermal stratification of the pre-eruptive magma chamber

Supporting Information:

Supporting Information may be found in the online version of this article.

Correspondence to:

A. B. Malaguti,
arianna.malaguti@ingv.it

Citation:

Malaguti, A. B., Scaillet, S., Pistolesi, M., Rosi, M., Speranza, F., & Renzulli, A. (2025). Coupled paleomagnetism and $^{40}Ar/^{39}Ar$ dating of latera ignimbrites (Vulsini Volcanic District, Italy) unravel processes associated to piston-collapse calderas. *Journal of Geophysical Research: Solid Earth*, *130*, e2024JB030910. https://doi.org/10.1029/2024JB030910

Received 3 DEC 2024
Accepted 3 AUG 2025

Author Contributions:

Conceptualization: Arianna Beatrice Malaguti, Stéphane Scaillet, Marco Pistolesi, Mauro Rosi, Fabio Speranza, Alberto Renzulli
Data curation: Arianna Beatrice Malaguti
Formal analysis: Arianna Beatrice Malaguti, Stéphane Scaillet, Fabio Speranza
Investigation: Arianna Beatrice Malaguti, Stéphane Scaillet, Marco Pistolesi, Mauro Rosi, Fabio Speranza, Alberto Renzulli
Methodology: Arianna Beatrice Malaguti, Stéphane Scaillet, Fabio Speranza

1. Introduction

Calderas are subcircular collapse structures resulting from rapid withdrawal of large volumes of magma from an underlying, shallow reservoir during either explosive or effusive eruptions (Acocella, 2021; Branney & Acocella, 2015; Cole et al., 2005). Calderas resulting from explosive eruptions generally host thick ignimbrite units accumulated during intra-eruption caldera sinking. Calderas are often polygenic in origin as a result of multiple collapses (Acocella, 2021), with overlapping structures and depositional units of different sources and ages. Identifying, correlating and dating such deposits is essential for accurately reconstructing the sequence and dynamics of individual caldera-forming events, as well as for assessing their recurrence and other key eruptive

Project administration: Mauro Rosi, Fabio Speranza, Alberto Renzulli
Resources: Stéphane Scaillet, Fabio Speranza
Supervision: Stéphane Scaillet, Marco Pistolesi, Mauro Rosi, Fabio Speranza, Alberto Renzulli
Validation: Arianna Beatrice Malaguti, Stéphane Scaillet, Marco Pistolesi, Mauro Rosi, Fabio Speranza, Alberto Renzulli
Visualization: Arianna Beatrice Malaguti, Stéphane Scaillet, Marco Pistolesi, Mauro Rosi, Fabio Speranza, Alberto Renzulli
Writing – original draft: Arianna Beatrice Malaguti, Stéphane Scaillet, Marco Pistolesi, Mauro Rosi, Fabio Speranza, Alberto Renzulli
Writing – review & editing: Arianna Beatrice Malaguti, Stéphane Scaillet, Marco Pistolesi, Mauro Rosi, Fabio Speranza, Alberto Renzulli

parameters such as intensity and volume. However, ignimbrites from a single eruption commonly display large-scale (or temporal) similarities in composition and lithology while varying in internal structure and depositional facies locally. This may hamper correlation of intra-caldera and outflow deposits distributed regionally across the caldera structure, or even across the temporal-depositional sequence itself. These shortcomings were identified by Hildreth and Mahood (1985) who reviewed several criteria (lithology, paleomagnetism, mineralogy/petrography, composition, and radiometric age) for the discrimination and correlation of ash-flow sheets, along with recommendations for their applicability based on characteristic features of the deposits (e.g., hardness, composition, sorting).

Over the past decades, progress in physical volcanology has considerably refined and expanded the spectrum of scenarios known to induce huge or abrupt lateral variations in ignimbrite lithology, depositional facies, and composition, both in proximal and distal facies (e.g., Branney & Kokelaar, 2002; Bear et al., 2009a, 2009b; Lipman, 1997; Pistolesi et al., 2016; Walker, 1983). These include: (a) instability of the eruption column due to transient changes of the vent/column dynamics; (b) interaction of step-wise sinking or tilting of individual blocks during caldera collapse with Pyroclastic Density Currents (PDCs) propagation and distribution (e.g., Branney & Kokelaar, 1992; Moore & Kokelaar, 1998; Valentine et al., 1992); (c) vertical compositional variation of eruption products (pumice and scoriae) due to magma tapping from a compositionally-zoned magma chamber (e.g., Branney & Kokelaar, 2002; Druitt et al., 2002; Fisher, 1990); (d) activation of multiple eruptive vents during ring-fault opening with sectorial emplacement of compositionally distinct PDCs; (e) changes in eruption intensity and distribution of PDCs inducing gaps (*hiatii*) in the eruptive sequence across the caldera structure; (f) proximal variations in depositional facies producing coarse agglomerate of scoriae or spatters grading vertically and laterally into lithic-rich breccias (Branney & Kokelaar, 2002) that are difficult to correlate to far-traveled, fines-rich, ash-flow sheets. Alone or in combination, these processes can seriously challenge the proper attribution of a given deposit to a specific eruptive event, especially in poorly exposed areas typical of huge, low-relief, caldera systems.

Paleomagnetic directional analysis is one of the most powerful tools to correlate ignimbrite deposits that is independent of lithology or depositional faces. When a lava or an ignimbrite cools below 580°C (Curie temperature of magnetite; Butler, 2004), it records the (paleo)magnetic direction aligned parallel to the local geomagnetic field direction (Korte et al., 2019; Lanza & Meloni, 2006). As cooling of a volcanic unit occurs, geologically, almost instantly (a few months or less), snapshots of the centennial-scale field directional variation called Paleo-Secular Variation (PSV; Griffiths, 2000; Korte et al., 2019) may thus be recorded by units erupted at different times. When tied to temporally calibrated PSV models (Pavón-Carrasco et al., 2014), highly resolved paleomagnetic analysis can thus provide a dating resolution in the order of one-two centuries, much better than routine radiometric methods. However, because the geomagnetic field oscillates around the same directions, similar paleomagnetic directions may repeat over centuries or millennia (Malaguti et al., 2022), requiring independent age control to verify if one or more cycles have been recorded.

PSV analysis as a correlation tool was pioneered by Gromme et al. (1972) and Bogue and Coe (1981) on ash-flow sheet in the Eastern Great Basin (Nevada and Utah, USA) and on Columbia River basalt flows (USA), respectively, and has been applied since the 1990s—often along with $^{40}Ar/^{39}Ar$ dating—to resolve stratigraphic correlation of ash-flow sheets showing similar lithological characteristics (e.g., Best & Christiansen, 1997; Best et al., 1995; Ort et al., 1999; Rotolo et al., 2021; Speranza et al., 2012; Stelten et al., 2018). The combination of radiometric dating with paleomagnetism represents in this case one of the best ways to resolve correlation and temporal variations by defining one (or more) temporal window(s) at the scale of a few millennia (or better) for which directional synchronicity at the scale below a few centuries can be assumed to hold.

Here we focus on the Quaternary Latera caldera (Vulsini Volcanic District, Italy), known as a world-class area for studying caldera-forming processes, and where some of the modern principles of physical volcanology were first established (Sparks, 1975). We address the correlation of two major units (the Grotte di Castro and the Onano Formations) through a systematic paleomagnetic and $^{40}Ar/^{39}Ar$ investigation on several key sites distributed across the caldera structure. Our study shows these two (formerly supposed) distinct units to actually belong to a single eruption, changing the perspective on the caldera dynamics. $^{40}Ar/^{39}Ar$ systematics are found to be tightly controlled by interactions between caldera collapse and eruption dynamics, illustrating the pitfalls inherent to $^{40}Ar/^{39}Ar$ dating of compound, sectorially variable, caldera-forming deposits. Taken together, our new data highlight the mechanisms and chronology of the caldera evolution, with broad implications for the study of similarly young Quaternary systems for which a millennial dating resolution can be achieved.

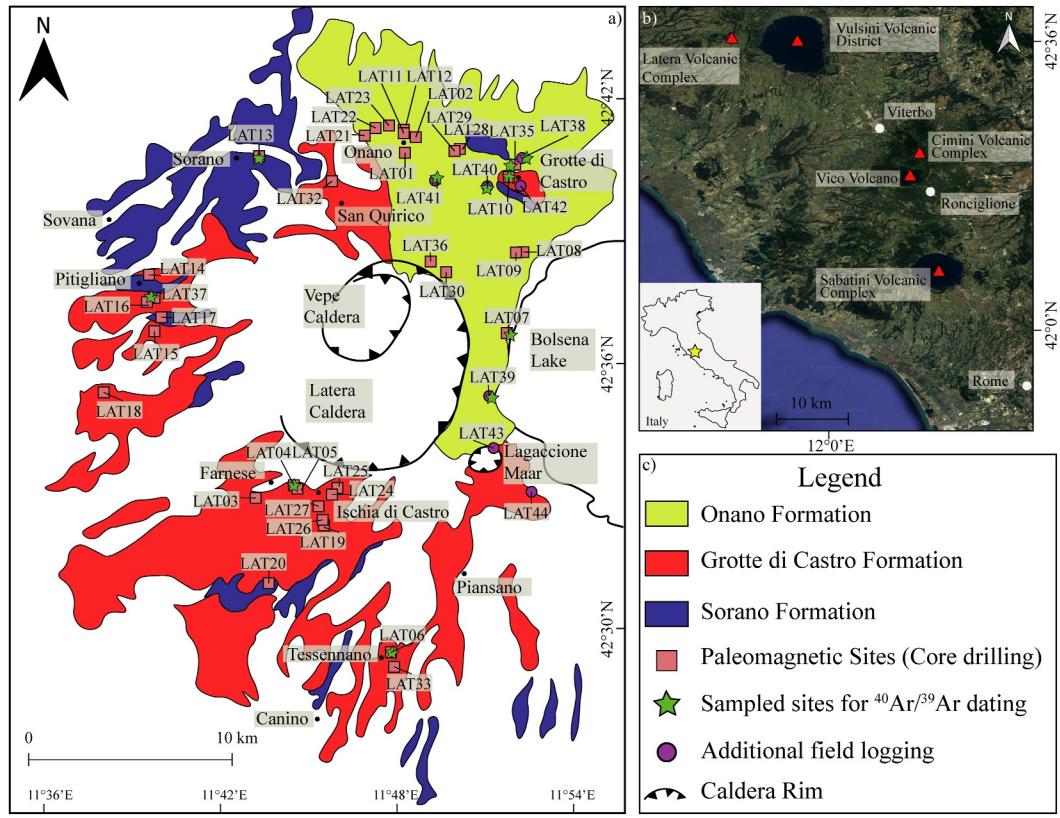

Figure 1. (a) Regional sketch map of the Latera Volcanic Complex with main depositional units (see inset for general location) and sampling paleomagnetic, $^{40}Ar/^{39}Ar$ sites, and additional field logging. The areal distribution of Onano Formation, Grotte di Castro Formation and Sorano Formation is modified from Metzeltin and Vezzoli (1983), Conticelli et al. (1987) and Vezzoli et al. (1987), Palladino et al. (2010, 2016). (b) Localization of the Latera Volcanic Complex, in relation to Latium volcanoes. (c) Legend of panel (a).

2. Latera Volcanic Complex: Caldera Structure and Ignimbrite Units

The Latera volcanic complex (hereafter LVC) is located in the western part of the Vulsini Volcanic District that was active from ca. 600 to 100 ka (Nappi et al., 1995; Palladino et al., 2010; and references therein; Figure 1 and Table S1 in Supporting Information S1). The early history of the LVC is characterized by pre-caldera lavas and Strombolian activity ranging between about 400 and 300 ka (Palladino et al., 2010). This activity was followed by several caldera-forming eruptions (Nappi, 1969a, 1969b; Palladino et al., 2010; Sparks, 1975) represented by moderate-size ignimbrite units emplaced in a time interval of about 120–90 kyr (ca. 280–250 to 160 ka; Brocchini et al., 2000; Marra, Bahain, et al., 2019; Marra, Costantini et al., 2019; Metzeltin & Vezzoli, 1983; Monaco et al., 2022; Nappi et al., 1995; Turbeville, 1992; Table S1 in Supporting Information S1). The volume of magma erupted during the whole explosive period can be estimated at >10 km^3 (Palladino et al., 2010). The last (minor) LVC caldera-forming eruptions gave rise to the well-preserved collapse structure of the nested Vepe Caldera in the NW sector of the main Latera caldera (Nappi & Renzulli, 1990; Nappi et al., 1991; Figure 1). Boreholes in the Latera caldera revealed a shallow, hypabyssal (subvolcanic) network of discontinuous leucite-bearing and syenite levels (apophyses) and skarns overlying a more continuous syenite intrusion about 2.2 km below the caldera floor (Barberi et al., 1984; Bertrami et al., 1984; Nappi et al., 1991).

The stratigraphic correlations and nomenclature of Latera ignimbrites have slightly changed since early studies (Table S1 in Supporting Information S1). Following the work of Vezzoli et al. (1987), the eruptive sequence is defined as Formations (Fm.) named from their type locality, from bottom to top: Canino Fm., Farnese Fm., Sovana Fm., Sorano Fm., Grotte di Castro Fm., Onano Fm., Tufi di Poggio Pinzo and Pitigliano Fm. (Figure S1 and Table S1 in Supporting Information S1).

Figure 2. (a) Basal contact of Sorano Fm.; (b) Basal fallout of Grotte di Castro Fm.; (c) Detail of surge deposit which hosts large holes left by flattened or entrained trees in the Grotte di Castro Fms.; (d) Detail of basal surges and sillar-type deposit of Grotte di Castro Fm.; (e) Sillar-type deposit of Grotte di Castro Fm. along the road cut to Pitigliano; (f) View of the sillar-type deposit of Grotte di Castro Fm. at Grotte di Castro. Refer to map in Figure 1a to match sample code with location of each field view.

2.1. Sorano, Grotte di Castro and Onano Ignimbrites

The Sorano ignimbrite consists of two (lower and upper) trachyte-phonolite PDC units (Palladino et al., 2010; Vezzoli et al., 1987; Figure 2a). The lower unit comprises a basal, up to 1 m-thick, crudely bedded, fine to medium ash and lapilli layers with alternating ash and pumice-lapilli beds (Valentine et al., 2019; Figure S1 in Supporting Information S1). The upper unit consists of a medium to poorly consolidated ignimbrite formed by light-colored pumices set in an abundant fine-to medium-ash matrix. Lithic clasts are rare, slightly increasing in content from base to the top (Valentine et al., 2019). The juvenile component consists of white to gray pumice lapilli containing sanidine phenocrysts, biotite, clinopyroxene and opaques (Conticelli et al., 1987). Available $^{40}Ar/^{39}Ar$ ages for the Sorano Fm. are consistent, between 194 ± 5 ka and 186 ± 20 ka (Marra, Bahain, et al., 2019; Turbeville, 1992; Table S1 in Supporting Information S1). Nappi (1969a, 1969b) was the first author to describe this formation, calling it "Lithoid Yellow Tuff" (Table S1 in Supporting Information S1).

The Grotte di Castro Fm. is a composite tephriphonolitic ignimbrite overlying a 0.5 m thick paleosol that in turn overlies the Sorano Fm. (Conticelli et al., 1987; Colucci et al., 2013; Palladino et al., 2010; Sparks, 1975; Figure 2b). The formation consists of multiple ignimbrite units exposed to the N, NW, and S of the caldera (Figure 1 and Figure S1 in Supporting Information S1). The deposits show significant lateral and vertical variations in lithic content, grain-size, and degree of hardening (Sparks, 1975). In the southern sector, the sequence rests on a brown paleosol, overlain by a Strombolian shoshonitic fallout deposit with plane-parallel stratification (Colucci et al., 2013), followed by a whitish pumice phonolitic lapilli layer rich in sanidine, green clinopyroxene and rare lithic clasts (fallout bed), and by a plane-parallel to low-angle, cross-bedded surge unit (Figure 2b; Conticelli et al., 1987; Colucci et al., 2013). In the western and northern sectors, the ignimbrite consists of a basal dune-bedded surge deposits hosting large holes left by flattened or entrained trees (Figures 2c and 2d). Occasionally, the fine ash beds are rich in mm-sized ash pellets set in a fine ash matrix (Sparks, 1975; Figure 2). Upwards, the stratigraphic sequence consists of a massive to diffuse bedded tuff, with rare sub-parallel granulometric layering, rich in igneous and sedimentary lithic clasts. Within a few km away from the caldera, the entire sequence is well consolidated ("sillar-type") and made of gray-colored pumice and scattered dark scoriae set in an abundant fine, brown-to yellow-colored matrix (Figures 2e and 2f; Sparks, 1975; Vezzoli et al., 1987). From geometric and spatial distribution evidence, the Grotte di Castro ignimbrite is inferred to lie below the Onano Fm., even if a direct (stratigraphic) contact between the two ignimbrites has never been observed (Marsella et al., 1987; Palladino & Simei, 2005; Sparks, 1975; Vezzoli et al., 1987). The available $^{40}Ar/^{39}Ar$ ages for the Grotte di Castro Formation are widely scattered between 225.3 ± 1.2 and 184.7 ± 8.7 ka (Marra, Costantini, et al., 2019; Monaco et al., 2022; Turbeville, 1992; Table S1 in Supporting Information S1).

According to several authors (Conticelli et al., 1987; Landi & D'Oriano, 2020; Nappi, 1969a, 1969b; Palladino & Simei, 2005; Sparks, 1975; Vezzoli et al., 1987), the Onano Fm. has a N and NE sectorial distribution (Figure 1). In the recent official Ispra geological map (https://www.isprambiente.gov.it/Media/carg/344_TUSCANIA/Foglio.html), it is also exposed to the E and SE of the LVC (Palladino et al., 2010, 2016). Landi and D'Oriano (2020) reconstruct the Onano succession as a sequence consisting of a partially eroded fallout (only found to the north of the Lagaccione Maar; Figures 1–3a), followed in the eastern and northern sectors by a well consolidated, dune-bedded, pumice-rich deposit, made by alternating massive and stratified ash layers and abundant white/yellowish ash matrix (Lower sillar; Figures 3a and 3c). Upwards, a slightly indurated, fines-poor breccia layer of about 1.5 m in thickness occurs, enriched in shallow to deeper (basement) lithics of sedimentary, thermometamorphic, subvolcanic, or hydrothermal origin (Lower lithic-rich breccia). The Lower lithic-rich breccia passes upwards to a reddish to black spatter-rich pyroclastic flow deposit (Spatter Unit; Figures 3d and 3f). Moving northwards away from the caldera, in the intermediate and distal parts, the Spatter Unit grades into an unconsolidated matrix-supported deposit, rich in scoria clasts. A peculiarity of the Spatter Unit is the presence of abundant fragments of crushed lithic material among (but also within) the juvenile clasts. Above it, a 5–6 m thick fines-poor breccia unit (Upper Lithic-rich Breccia; Figure 3d) occurs mostly made of lithics of volcanic and sedimentary rocks, whereas juvenile clasts are scarce. In the intermediate and distal parts, the Upper Lithic-rich Breccia laterally grades, away from the caldera to a well-consolidated ignimbrite (Upper sillar; Figures 3e and 3f). The deposit is characterized by at least two different types of mixed/mingled juvenile material, from phonolite to phonotephrite in composition (Landi & D'Oriano, 2020), including black scoriae and white/yellowish to gray pumiceous lapilli. According to Palladino and Simei (2005) and Landi and D'Oriano (2020), the Upper Sillar was emplaced during the eruption climax. An $^{40}Ar/^{39}Ar$ age estimate is given for this formation by Monaco et al. (2022) at 224.7 ± 2.6 ka (Table S1 in Supporting Information S1).

3. Materials and Methods

3.1. Paleomagnetism

During February–June 2021, paleomagnetic sampling was carried out at 35 sites (357 oriented paleomagnetic cores, LAT code; Figure 1 and Table 1), focusing on the yellowish-colored, sillar-type, tuff matrix ignimbrite attributed to the Grotte di Castro and Onano Formations. In addition, the older Sorano Fm. was sampled for paleomagnetic characterization. The paleomagnetic correlation method was applied following previous work based on comparing the paleomagnetic directions from medium to hardly consolidated ash flow tuff deposits (e.g., Bogue & Coe, 1981; Grommé et al., 1972; Ort et al., 1999, 2013; Speranza et al., 2012).

Figure 3. (a) Detail of the Onano basal fallout deposit; (b) Lower Sillar deposit of Onano Fm.; (c) Lower Sillar deposit of Onano Fm.; (d) Spatter Unit and Upper Lithic-rich Breccia deposits of Onano Fms.; (e) Spatter Unit and Upper Sillar deposits of Onano Fm.; (f) Spatter Unit and Upper Sillar deposits of Onano Fm. Refer to map in Figure 1a to match sample code with location of each field view.

It has been shown that sometimes the paleomagnetic directions from the same volcanic units have 95% confidence cones that do not overlap (e.g., Branca et al., 2019; Magli et al., 2021, 2024; Malaguti et al., 2023; Pistolesi et al., 2021; Risica et al., 2019; Speranza et al., 2006). This may be due to several factors, predominantly local magnetic anomalies (Baag et al., 1995), and/or local post-cooling tilting (Lanza & Zanella, 2006; Speranza et al., 2006, 2012).

There are several checks for determining whether two data sets share a common mean direction. The most standard approach is Watson's F test (Watson, 1956), or (preferably) the Watson V_w Test (Watson, 1983), for determining whether two Fisher distributions of directions are statistically distinct. In the latter, two data sets share a common mean direction (i.e., are unresolved) when the statistical parameter V_w (which increases as the difference between the mean directions of the two data sets increases) is smaller than a critical value (V_{crit}) determined through Monte Carlo simulation (Tauxe et al., 2016).

Table 1
Mean Paleomagnetic Directions From Latera Ignimbrite and Scoriae Deposits

Volcanic unit	Code	n/N	Latitude, °N	Longitude, °E	D, deg	I, deg	k	α_{95}, deg
Onano Spatter Unit	LAT01	9/10	42°41′15.30″N	11°48′40.92″E	344.6	47.1	197.1	3.7
Onano Upper Sillar[a]	LAT02	0/10	42°41′42.18″N	11°48′59.62″E	/	/	/	/
Grotte di Castro	LAT03	5/10	42°32′45.08″N	11°43′15.50″E	340.3	44.5	100.6	7.7
Grotte di Castro[a]	LAT04	0/10	42°33′3.36″N	11°44′32.70″E	/	/	/	/
Grotte di Castro[a]	LAT05	8/10	42°32′59.50″N	11°44′37.27″E	355.1	40.3	11.4	17.1
Grotte di Castro	LAT06	6/10	42°28′48.53″N	11°47′40.07″E	337.3	54.3	95.7	6.9
Onano Spatter Unit	LAT07	7/10	42°36′40.63″N	11°51′55.00″E	332.9	51	256.2	3.8
Onano Upper Sillar	LAT08	9/10	42°38′40.57″N	11°52′34.40″E	351.7	46.6	268.5	3.1
Onano Spatter Unit	LAT09	10/10	42°38′42.05″N	11°52′20.46″E	350.9	43.2	284.9	2.9
Grotte di Castro	LAT10	10/10	42°40′31.70″N	11°52′11.57″E	338.1	53.4	235.6	3.2
Onano Upper Sillar	LAT11	7/10	42°41′44.97″N	11°48′40.34″E	357.8	61.4	346.8	3.2
Onano Upper Sillar[a]	LAT12	8/10	42°41′49.19″N	11°48′39.73″E	2.6	42.4	269.7	3.4
Sorano[a]	LAT13	0/13	42°41′18.10″N	11°43′46.86″E	/	/	/	/
Grotte di Castro[a]	LAT14	10/10	42°38′11.10″N	11°39′48.64″E	320.8	42.9	2.6	36.9
Grotte di Castro[a]	LAT15	10/10	42°37′3.17″N	11°40′3.43″E	4.8	51.8	22.2	10.5
Grotte di Castro[a]	LAT16	10/10	42°37′47.76″N	11°39′46.68″E	31.7	42.9	3.2	31.9
Sorano[a]	LAT17	0/13	42°37′13.25″N	11°40′19.01″E	/	/		/
Grotte di Castro[a]	LAT18	8/10	42°35′31.94″N	11°38′13.35″E	356.4	66.8	3.3	36.2
Grotte di Castro[a]	LAT19	5/10	42°32′3.08″N	11°45′29.65″E	358.8	53.7	43	11.8
Sorano[a]	LAT20	0/13	42°30′50.74″N	11°43′19.95″E	/	/	/	/
Onano Upper Sillar	LAT21	8/10	42°41′35.21″N	11°47′9.99″E	351.5	48.6	178.7	4.2
Onano Upper Sillar	LAT22	10/10	42°41′54.13″N	11°47′42.92″E	337.6	56	254.7	3
Onano Upper Sillar	LAT23	10/10	42°41′55.28″N	11°48′13.76″E	356.4	57	262.2	3
Grotte di Castro[a]	LAT24	4/10	42°32′45.77″N	11°45′46.46″E	326.9	42	2.8	67.8
Grotte di Castro[a]	LAT25	7/10	42°32′52.49″N	11°45′54.35″E	348.9	57.6	10.7	19.3
Grotte di Castro	LAT26	5/10	42°32′11.62″N	11°45′26.96″E	342.9	54.4	289.07	4.4
Grotte di Castro[a]	LAT27	0/10	42°32′28.84″N	11°45′21.16″E	/	/	/	/
Onano Upper Sillar	LAT28	6/10	42°41′18.67″N	11°50′31.39″E	1	50	681.7	2.6
Onano Upper Sillar[a]	LAT29	0/10	42°41′12.76″N	11°50′21.51″E	/	/	/	/
Onano Spatter Unit	LAT30	6/10	42°38′13.26″N	11°49′55.43″E	332.8	60.9	174.2	5.1
Grotte di Castro	LAT32	9/10	42°40′37.60″N	11°46′8.92″E	350.8	52	555.9	2.2
Grotte di Castro	LAT33	8/10	42°28′25.00″N	11°47′44.18″E	340.4	60.8	195	4
Onano Upper Sillar	LAT35	6/9	42°40′41.42″N	11°52′22.41″E	352.8	52.9	147.5	5.5
Onano Upper Sillar[a]	LAT36	9/9	42°38′30.03″N	11°49′24.94″E	332.6	56.5	11.3	16
Grotte di Castro	LAT37	8/10	42°37′50.31″N	11°39′51.32″E	359.7	61.9	158.2	4.4
Grotte di Castro Sample mean		51/67			344.3	55.2	86.2	2.2
Onano Sample mean		89/108			348.6	52.2	76.4	1.7

Note. Latitude and Longitude of the sites were collected by a Garmin GPS, using theWGS84 datum. n/N is number of Characteristic Remanent Magnetization (ChRM) directions utilized to calculate the site-mean direction/total number of cores drilled at a site, or number of ChRM directions utilized to calculate the volcanic unit-mean direction/total number of cores drilled in the volcanic unit. D, deg is paleomagnetic declination, I, deg is inclination, α_{95}, deg and k are statistical parameters after Fisher (1953). [a]Discarded sites with MAD values > 15° or α_{95} > 10°(see text).

At each site, we drilled 10–13 cores (2.5 cm of diameter) using a petrol-powered portable drill cooled by water. We spaced the cores evenly across local exposures and outcrops to obtain a well-averaged and representative paleomagnetic direction for each volcanic unit. Both a magnetic and a sun compass were used to orient all cores in situ. The magnetic compass was set considering a ∼3° regional geomagnetic declination (https://www.ngdc.noaa.gov/geomag/calculators/magcalc.shtml#declination). The local field declination values (i.e., the difference between the magnetic and sun compass readings) are predominantly negative and vary from −7.8° to 10.9° (average 0.2°).

The Natural Remanent Magnetization (NRM) of the samples was measured in the shielded room of the paleomagnetic laboratory at Istituto Nazionale di Geofisica e Vulcanologia (Roma), by a 2G Enterprises direct current, Super-conducting Quantum Interference Device (SQUID) cryogenic magnetometer. Alternating field (AF) demagnetization was performed on all samples, using 11 demagnetization measurement steps up to a maximum field of 120 mT. Orthogonal diagrams (Zijderveld, 1967) and equal-area projections were used to plot the AF demagnetization data, whereas the magnetization components were isolated by principal component analysis (Kirschvink, 1980). Fisher's (1953) statistics were used to calculate mean paleomagnetic directions for each site.

3.2. Petrography

A total of 23 representative thin sections were examined from both the ignimbrite matrix (10) and the individual juvenile clasts (13) for mineralogic-petrographic investigations as well as to provide guidance in mineral separation for $^{40}Ar/^{39}Ar$ dating, based on freshness and typology of crystals. Zellmer's (2021) genetic terminology of crystals in volcanic rocks (phenocrysts vs. antecrysts–xenocrysts) was used to relate texture and crystal typology to within-chamber magma processes operating prior (or leading) to eruption (e.g., mixing, mingling, fractional crystallization, degassing-fragmentation).

The dominant mineralogical assemblage of the Grotte di Castro and Onano deposits consists of plagioclase (Plg), sanidine (San) and leucite (Lc) among the sialic fundamental phases and clinopyroxene (Cpx), biotite (Bt) and rare olivine among the mafic ones. Among the accessory phases the opaque minerals (Opq), mainly magnetite, are commonly present whereas apatite is rare. Leucite or sanidine antecrysts/glomeroantecrysts, trachyte-to syenite/microsyenite and sedimentary-xenoliths in a vesiculated glassy groundmass also occur (Figure 4). The Porphyritic Index of the juvenile component (P.I. = total phenocrysts abundance expressed as volume %, not vesicles-corrected) ranges between 1 and 3 vol.%.

In agreement with Landi and D'Oriano (2020), the investigated pyroclastic products of the Grotte di Castro and Onano Formations are crystal-poor, often with minerals not in equilibrium with the erupted magma. As all the products belonging to the final explosive events of the LVC eruptions, they show a compositional heterogeneity from phonotephrite to phonolite, which reflects the combined effects of fractional crystallization and magma mixing/mingling between the two compositional end-members, without implying a specific temporal sequence between the two processes. This heterogeneity indicates that the magmatic reservoir was periodically affected by the arrival of less evolved (more primitive) magmas. The simultaneous withdrawal of magma from different portions of the magmatic reservoir disrupts the pre-eruptive chemical zoning and gives rise to a complex phase relationships among the mineral populations (Landi & D'Oriano, 2020). By contrast, the early stage of the ignimbrite-forming eruptions of the LVC was dominated by trachytes to phonolites (with a weak compositional zoning) whose involvement, as xenocrysts, in the younger caldera-forming eruptions cannot be however ruled out.

3.3. $^{40}Ar/^{39}Ar$ Sampling Criteria and Methods

Eleven sites were selected for $^{40}Ar/^{39}Ar$ dating (Figure 1) for which thin section petrographic observations revealed the presence of fresh sanidine phenocrysts, a key target for $^{40}Ar/^{39}Ar$ dating. Fresh leucite phenocrysts (unreacted to analcime) were also selected. The occurrence in thin section of leucites with thin feldspar rims, probably due to peritectic reactions on antecrysts (Figure 4d), suggests these may have been hand-picked as well.

Total-fusion and step-heating $^{40}Ar/^{39}Ar$ dating was performed on sanidine and leucite single crystals from single or multiple juvenile pumice clasts from 11 samples. Where the individual pumices or scoriae were too small, crystal-poor or aphyric, the ignimbrite matrix was sampled. The samples were crushed, sieved and sanidine and leucite crystals hand-picked from the 1.0–0.5 mm fraction under a binocular microscope. These were

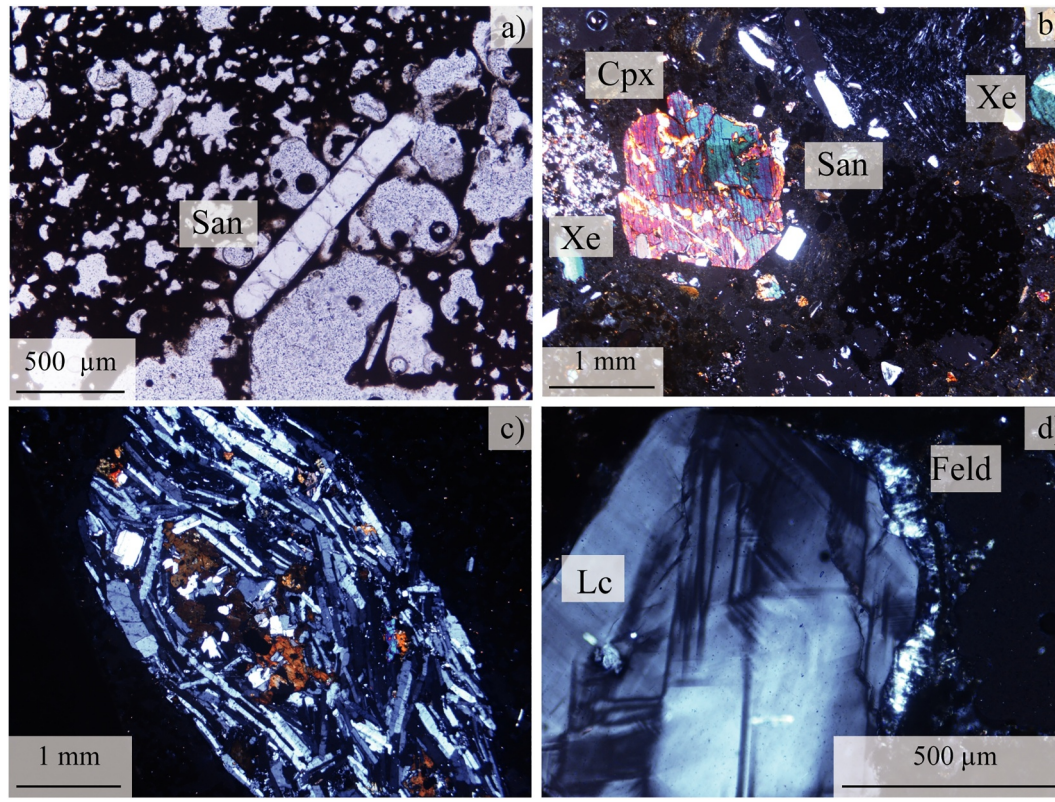

Figure 4. Thin section images in Plane Polarized Light (PPL) or Crossed Nichols (NX) of representative samples. (a) (PPL) and (b) (NX): LAT04 showing sanidine phenocrysts (San, a), clinopyroxene (Cpx, b), broken sanidine antecrysts (San, b) and various kind of xenoliths (Xe, b); (c–d) (NX): LAT40 showing a rounded trachyte to microsyenite autolith/xenolith (c) and a large-size leucite (Lc) antecryst with feldspar (Feld) reactions (d).

ultrasonically washed in cold HF 5% to ensure the highest purity. They were wrapped and stacked in two separate irradiation cans and irradiated for 5 min (CLICIT) or 36 min (CLOCIT) in the Cd-lined, inner-core and outer-core slot positions of the Corvallis Nuclear Reactor (Oregon State University, USA) along with the ACR (Alder Creek Rhyolite) and FCT (Fish Canyon Tuff) sanidine standards, respectively with the recommended nucleogenic production ratios in Niespolo et al. (2017) and Phillips et al. (2017). $^{40}Ar/^{39}Ar$ dating was performed at Institut des Sciences de la Terre d'Orléans (ISTO, CNRS-Orléans) using a high-resolution Helix SFT mass spectrometer outfitted to a home-built CO_2-laser based extraction system featuring ultra-low argon blanks (Corti et al., 2019; Franceschini et al., 2020). Total-fusion or step-heating was applied according to weight, and individual fusion and step ages were calculated according to Scaillet (2000) with all ages quoted at ± 1σ. The number of heating steps was generally above 15 (Table S2 in Supporting Information S1). Decay and isotopic constants used are those as listed in Steiger and Jäger (1977) and McDougall and Harrison (1999).

Two different summary statistics are reported, the Total Gas Age (TGA) and a MSWD-filtered weighted mean age estimate (hereafter "MSWD-F" estimate). The TGA is calculated by individually summing each Ar isotope over all individual analyses (total fusion or step-heating fractions), then using the totals to compute a nominal K-Ar age with an error derived by quadratic error propagation of the individual errors through the age equations. Alternatively, the MSWD-F estimate (e.g., Gansecki et al., 1996; Stelten et al., 2015) is based on identifying the most probable juvenile component nominally defined as the more compact "youngest" weighted mean consistent with a Normal distribution. See discussion in Schaen et al. (2020). The MSWD-F estimate is determined by sequentially pooling the individual ages sorted by increasing value until the normalized Mean Square of Weight Deviation (MWSD/(N-1)) falls outside the fiducial range for the corresponding χ^2 statistics for N-1 degrees of freedom (where N is the number of data included; Gansecki et al., 1996; Wendt & Carl, 1991). Technically, MSWD-F retains the youngest compact set that is internally consistent within analytical error considering that geologic scatter below this level simply cannot be resolved. Between-sample variations in MSWD-F essentially

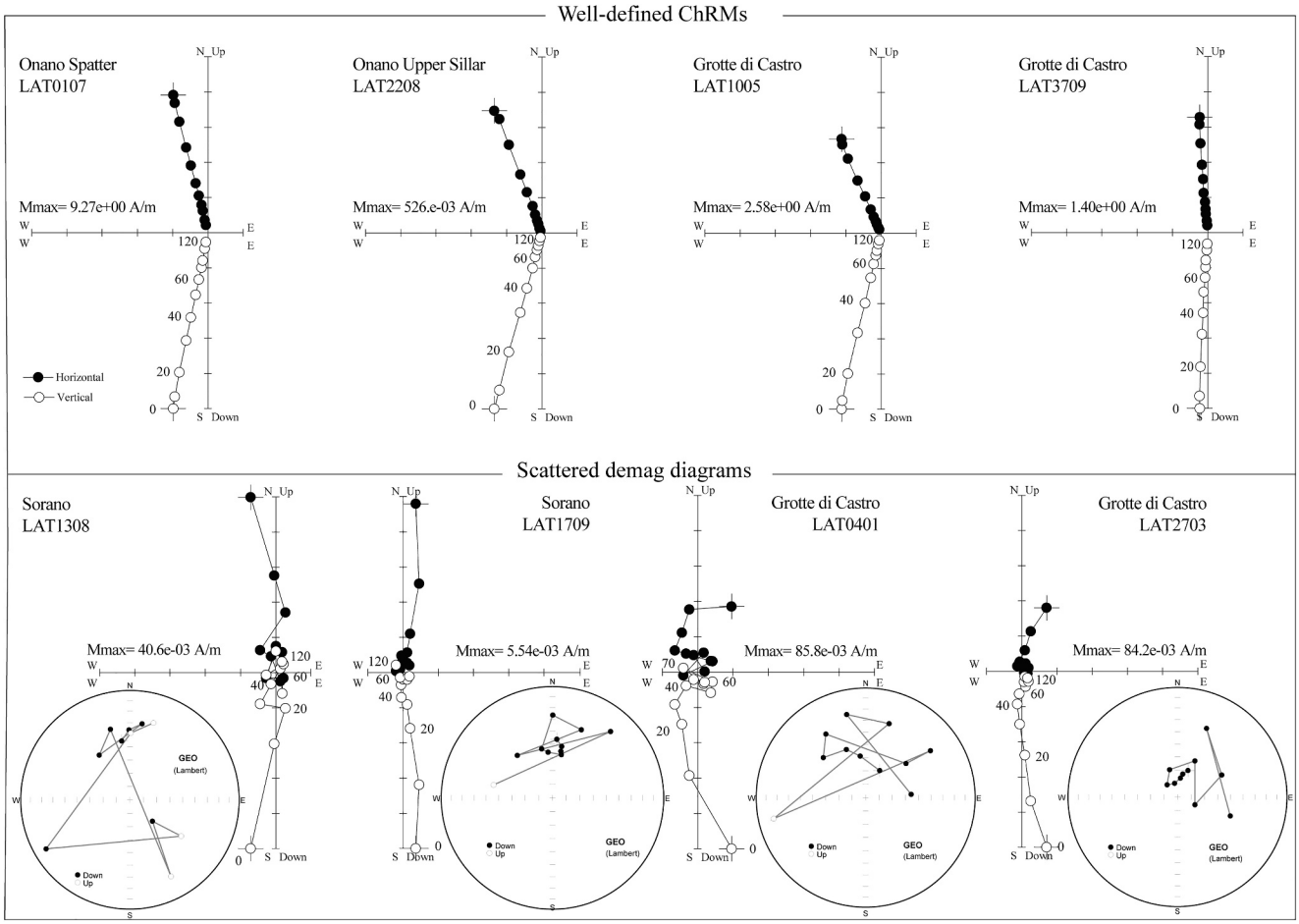

Figure 5. Representative orthogonal vector and equal-area projection diagrams of typical alternating field demagnetization data of samples drilled in volcanic matrix and scoriae, in situ coordinates. Open and solid dots represent projections on the vertical and horizontal planes, respectively. Demagnetization step values are in mT.

flag excess scatter resolved beyond χ^2 confidence limits, but not the source of this scatter. A dedicated maximum-likelihood estimate (MLE) is implemented further below which specifically addresses the identification of a most probable juvenile component among samples from the same units affected by variable excess scatter due to variable proportion of xenocrystic/autocrystic pre-eruptive ages. Isochron data are plotted and reported (Table S2 and Figure S3 in Supporting Information S1) and indicate the presence of atmospheric trapped argon in the vast majority of cases.

In the data calculation and interpretation hereafter, we follow the guidelines and procedures established and published time ago in Scaillet (2000), Scaillet and Guillou (2004) and Scaillet et al. (2011, 2013), regarding notably the dating of very young pyroclastic products. These describe and implement in much greater detail than more recent accounts (e.g., Schaen et al., 2020) central aspects of error handling not explicitly addressed elsewhere.

4. Results

4.1. Paleomagnetic Directions

AF demagnetization data reveal that 11 out of 15 sites (73%) from the Onano Fm. (4 from welded scoriae of the Spatter unit and 7 from tuff matrix of the Lower and Upper Sillar deposit) and 7 out of 17 sites (41%) from the Grotte di Castro Fm. (all from tuff matrix, except for the black welded scoria LAT37 site) yield a well-defined ChRM in the 30–120 mT interval (Figure 5 and Table 1). All samples yielding maximum angular deviation value calculated by demagnetization data (MAD) greater than 15 or an $\alpha_{95} > 10°$ were considered to be scattered and

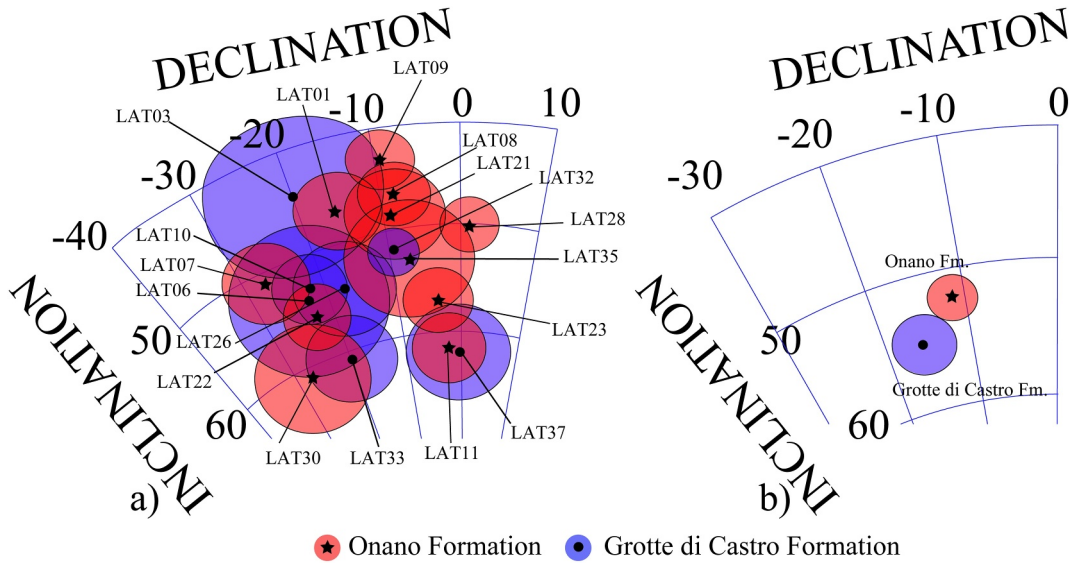

Figure 6. Equal-area projection (lower hemisphere) of (a) site-mean and (b) sample mean paleomagnetic directions from Grotte di Castro and Onano Fms. (Latera volcano). The ellipses around the paleomagnetic directions are the projections of the relative α_{95} cones. All the paleomagnetic directions are listed in Table 1.

excluded from the analysis, ensuring an objective criterion for data selection. Finally, site LAT12 was excluded from the analysis because it belonged to another geological formation. The well-defined site-mean declinations vary from 332.9° to 1.0°, while inclinations are between 43.2° and 61.9° (Figure 6 and Table 1). The α_{95} values relative to the well-defined site-mean paleomagnetic directions vary from 2.2° to 7.7°, with 4.05° on average.

On the other hand, 10 sites from the Grotte di Castro Fm. (59%; all from matrix), 4 (26%; all from matrix) from the Onano Fm. (Upper Sillar) and the three sites from the Sorano Fm. (all from matrix), do not show a well-defined ChRM, that is after the elimination of a viscous component at 20–30 mT, the demagnetization diagrams are scattered or erratic (Figure 5 and Table 1).

4.2. $^{40}Ar/^{39}Ar$ Results

$^{40}Ar/^{39}Ar$ results for the 11 sampling sites (Figure 1) are presented as age spectra (step-heating analyses, SH), age-ordered spectra (total-fusion, TF; Figures 7–9) and stacked density plots and Table S2 in Supporting Information S1. The $^{40}Ar/^{39}Ar$ data are individually tabulated for each sample in Supporting Information S1. Table 2 reports a summary listing of the age estimates obtained from the sanidine and leucite crystals separated from both the juvenile clasts and the tuff-matrix. The age range (dubbed Spread) covered by each data set and associated bounds are summarized in Table 3.

The data are discussed first separately (by site), then collectively (by unit) using a common age-ordered spectrum plot lumping all corresponding data in Figure 7. This allows direct visualization of the overall age range (and variability) internally recorded in each depositional unit.

Grotte di Castro Fm. (LAT06, LAT10, LAT37, LAT04). Four sites belonging to the Grotte di Castro Fm. were analyzed by the total fusion procedure. At site LAT06, sanidine crystals were separated from both the matrix and the juvenile scoria, to investigate possible age differences between the two. The results for the matrix and the scoriae are similar with a $^{40}Ar/^{39}Ar$ age distribution ranging from about 132 to 282 ka (Table 3). MSWD-F estimates are indistinguishable at 211.3 ± 1.5 ka (in matrix) and 212.9 ± 1.6 ka (in juvenile scoria; Table 2 and Table S2 in Supporting Information S1). Pooled together, these return a common MSWD-F estimate at 213.2 ± 1.1 ka (Table 2). Note that the youngest (discarded) ages are visibly associated with anomalously high atmospheric contamination, the reason for their exclusion. A broadly similar $^{40}Ar/^{39}Ar$ distribution was obtained between 194 and 275 ka for LAT10 matrix and LAT37 scoriae, with a MSWD-F of 213.2 ± 1.0 ka and 214.7 ± 1.1 ka, respectively (Table 3). Pumice clasts of sites LAT04 produced a single-crystal $^{40}Ar/^{39}Ar$ distribution from 163 to 230 ka, with a MSWD-F age of 211.0 ± 0.9 ka (Table 3 and Table S2 in Supporting

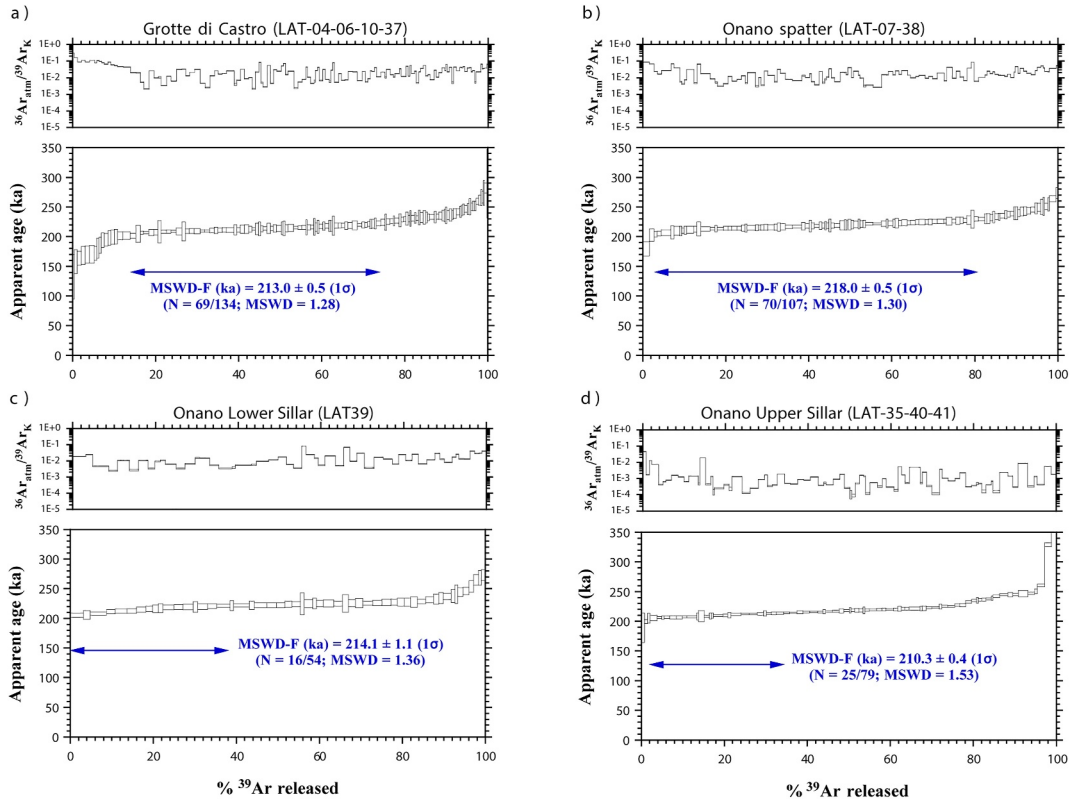

Figure 7. $^{40}Ar/^{39}Ar$ sanidine data from (a) Grotte di Castro, (b) Onano Spatter, (c) Onano Lower Sillar and (d) Onano Upper Sillar. Each panel for each unit illustrates the argon isotopic composition of the released gas, as labeled (upper three spectra), and the age-ordered spectrum along with the MSWD-F estimate calculated over the fractions spanned by the arrow. n/N indicates the number of analyses included (over the total).

Information S1). Considered together, all samples from this unit provide a pooled MSWD-F estimate at 213.0 ± 0.5 ka (Figures 7a and Table 2) that is internally consistent with the individual estimates.

Leucite was also analyzed by step heating and total fusion of single crystals from LAT37 scoriae with the aim to compare with the companion sanidines. Step heating experiments yielded homogeneous spectra (Figure 8), yet with plateaus either consistent (217 ± 3 ka, Leucite #2) or significantly older (225 ± 3 ka, Leucite #1; 237 ± 4 ka, Leucite #3) than the companion sanidine (Table 2). Note that the older ages fall in the range of the oldest sanidine ages measured at this site.

Onano Fm. (LAT39, LAT07, LAT38, LAT35, LAT40, LAT41). The single-grain $^{40}Ar/^{39}Ar$ results for the six sites of Onano Fm. are equally scattered as for Grotte di Castro Fm. Sanidine crystals from the pumice clasts at the base of Lower Sillar of the Onano Fm. (LAT39) range from about 205 to 273 ka, with a MSWD-F age of 214.1 ± 1.1 ka (Table 3 and Table S2 in Supporting Information S1). Sanidine crystals extracted from scoria clasts of the Spatter Unit of the Onano Fm. (LAT07 and LAT38; Figure 7b). yielded $^{40}Ar/^{39}Ar$ ages ranging from 180 up to 273 ka, with a MSWD-F estimate 216.3 ± 0.9 ka (LAT07) and 219.3 ± 0.6 ka (LAT38), measurably older than for Onano Lower Sillar (Table 2). Pooled together, these also return to an older, common, MSWD-F age at 218.0 ± 0.5 ka (Figure 7c and Table S2 in Supporting Information S1). Finally, the sanidine crystals from the matrix of the Upper Sillar (LAT35, LAT40, LAT41) show a wider age distribution from 189 to 260 ka, yet with a MSWD-F estimate systematically younger than recorded elsewhere (LAT35: 207.0 ± 0.9 ka; LAT40: 210.7 ± 0.7 ka; LAT41: 207.0 ± 0.9 ka; Table 2), collectively pooling to 210.3 ± 0.4 ka (Figure 7d and Table S2 in Supporting Information S1), as obtained by recombining the single crystal data sets and redoing the MSWD-F analysis.

As with the Grotte di Castro Fm., step-heating (SH) and total-fusion (TF) analyses were conducted on individual leucite crystals to compare with the sanidine ages of the same samples. These again yielded homogenous but variable plateaus systematically older than the companion sanidine for Onano spatter (scoria clasts LAT07:

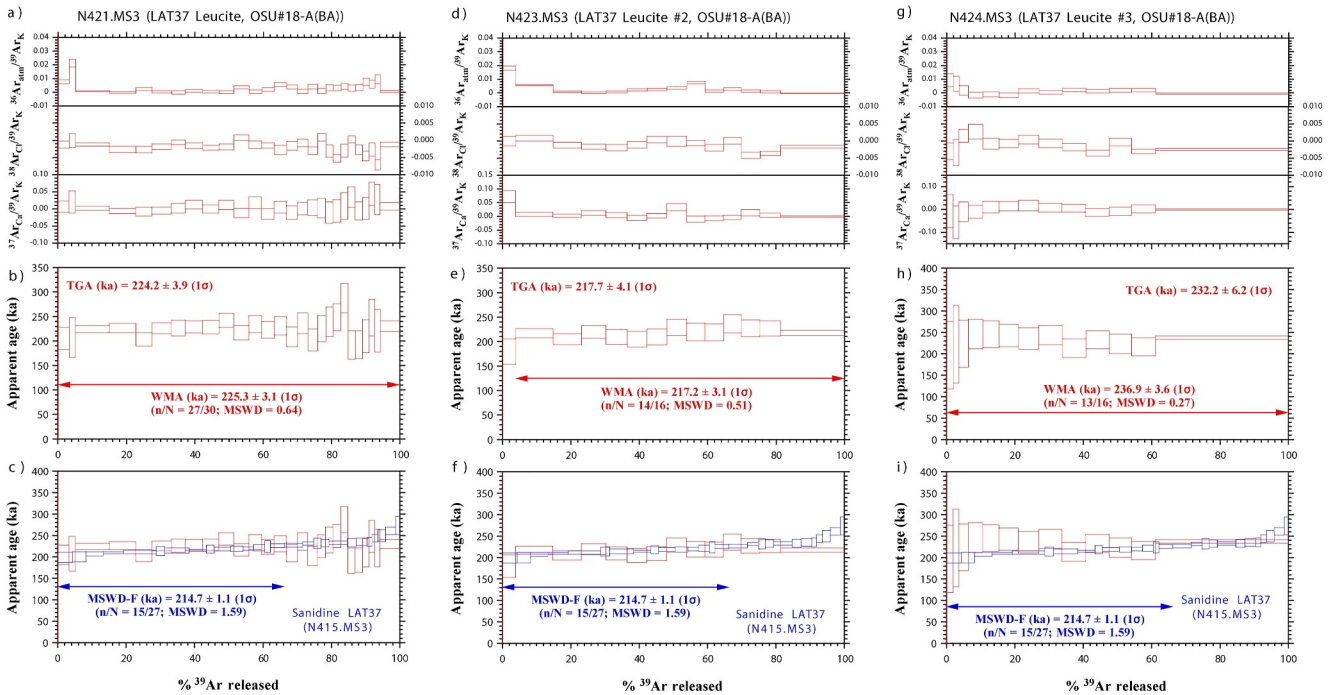

Figure 8. Step-heating Ar/Ar spectra from single leucite crystals of Grotte di Castro (LAT37). Each panel illustrates: (a, d, g) the isotopic composition of the released gas; (b, e, h) the age release spectrum with Total Gas Age and WMA indicated; (c, f, i) the age spectrum overlapped with the corresponding age-ordered sanidine data. n/N indicates the number of fractions included (over the total analyzed).

233 ± 4 ka, Leucite #1; 242 ± 5 ka, Leucite #2; 241 ± 6, Leucite #3; Table 2). This contrasts with the leucite ages of Onano Upper Sillar that are variable but on average more consistent with the younger sanidine ages round 210 ka (Table 2).

Sorano Fm. (LAT13). Sanidine crystals extracted from Sorano Fm. pumice clasts at site LAT13 (Figure 9) were analyzed to cross-check $^{40}Ar/^{39}Ar$ ages with stratigraphic evidence that this unit is older than Grotte di Castro and Onano Formations. The single-grain $^{40}Ar/^{39}Ar$ sanidine ages yielded a distribution on average much flatter than all other samples of either Onano or Grotte di Castro Fms., with a MSWD-F estimate at 220.2 ± 1.1 ka for over most of the corresponding distribution (Figure 9 and Table S2 in Supporting Information S1).

5. Discussion

5.1. Paleomagnetic and $^{40}Ar/^{39}Ar$ Sanidine Constraints

AF demagnetization carried out on welded scoriae and yellowish-colored tuff matrix from Grotte di Castro and Onano Fms. provide evidence of mutually consistent (hence spatially correlative) paleomagnetic directions, with well-defined ChRMs (Figure 5 and Table 1). Whereas all data obtained from Sorano samples were discarded as they did not yield well-defined ChRMs (see scattered demag diagram in Figure 5 and Table 1).

We applied Watson's V_w test, using the PmagPy function of Tauxe et al. (2016), to the paleomagnetic directions of Onano and Grotte di Castro to test whether these two data sets share a common mean value. The returned V_w score (1.7) is smaller than V_{crit} (6.8) (Figure S2 in Supporting Information S1), indicating a common (or unresolved) mean direction. According to Pavón-Carrasco et al. (2009), European geomagnetic and archeomagnetic data indicate that, over the past 3,000 years, the geomagnetic field has varied by up to 7° every 100 years in the central Mediterranean. If valid further back in time, this translates into a time-span resolution around 100–200 years for directional data differing by less than 2–4°, as applies here, indicating a depositional time spanning a 100–200 yr interval at most.

Regarding the $^{40}Ar/^{39}Ar$ constraints, one primary observation from the sanidine data is that none of the samples produced a fully internally consistent distribution with a single homogenous mode spanning the entire data spread

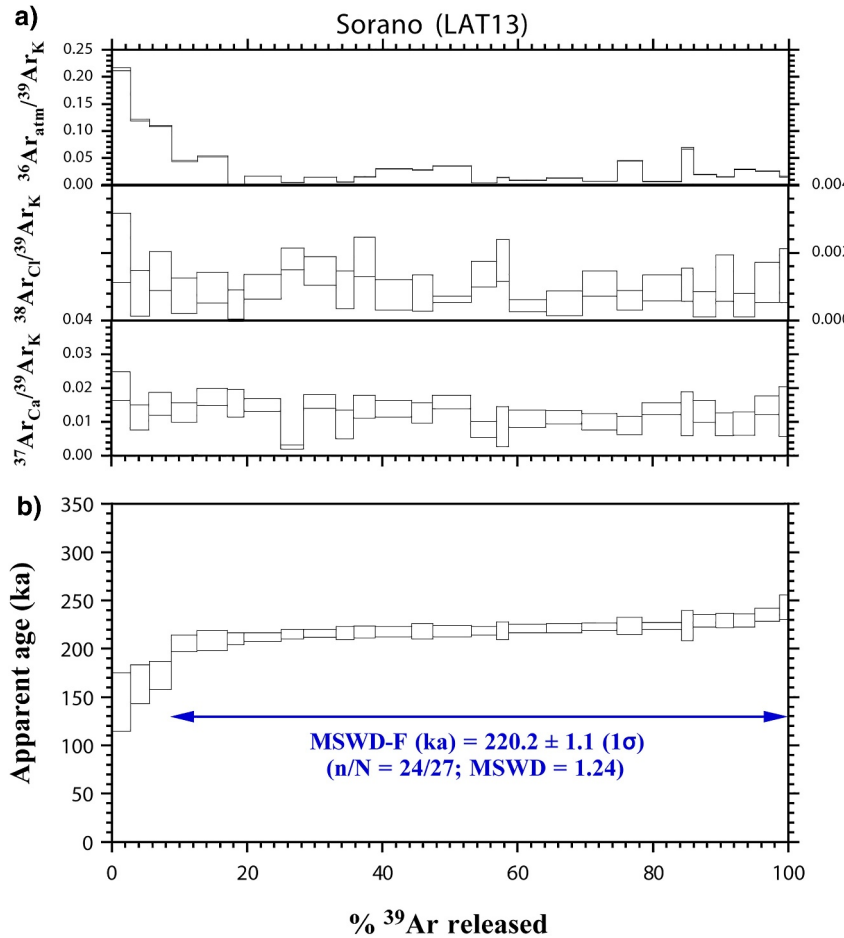

Figure 9. Age-ordered spectrum of total-fusion single-grain $^{40}Ar/^{39}Ar$ sanidine data of Sorano (LAT13). Each panel illustrates the: (a) isotopic composition of the released gas; (b) MSWD-F estimate computed discarding the younger (distinctly atmos-contaminated) ages (see upper plot). n/N indicates the number of analyses included (over the total).

(with the exception of Sorano Fm., discussed later). All samples display variable but systematic internal age variations spanning 45–50 kyr, and up to 100 kyr (LAT06, Grotte di Castro; Table S2 in Supporting Information S1 and Table 3). As noted before, young outliers may be found in some samples, but these are distinctly flagged by a higher air contamination $^{36}Ar_{atm}/^{39}Ar$ ratio (in particular for Grotte di Castro; Figure 7a). These are not considered further except to remind the circumstance where appropriate.

A second observation is that the age variability internal to each sample is almost continuous between the youngest and oldest components recorded, excluding a few and clearly erratic old ages (notably in the Onano Upper Sillar pool; Figure 7c and Table S2 in Supporting Information S1). There is no gap nor prominent step in the age-ordered spectra to suggest a component distinctly older than the youngest (juvenile) mode. This is common to all samples, except for Sorano Fm. that retains a compact distribution across the whole spectrum of apparent ages (Figure 9). Such a smooth, sub-continuous, age distribution is quite distinct from erratic $^{40}Ar/^{39}Ar$ patterns typically expected from accidental contamination by older true xenocrysts (e.g., Gansecki et al., 1996; Phillips et al., 2023; Rivera et al., 2016), calling for another cause to explain the regular progression recorded in each pooled spectrum (Figure 7).

Going down to the scale of individual samples, we note a broad consistency in internal $^{40}Ar/^{39}Ar$ sanidine systematics, especially regarding the juvenile MSWD-F estimates derived between sites belonging to the same unit (Table 2). These agree particularly well for the Grotte di Castro samples that all fall within uncertainty of each other at 213.0 ± 0.5 ka (= their pooled MSWD-F estimate, Figure 7a). Slightly less compact (but nearly so) is the MSWD-F estimates of Onano Upper Sillar clustering between 207 and 212 ka (pooling at 210.3 ± 0.4 ka,

Table 2
Summary of $^{40}Ar/^{39}Ar$ Age

Run#	Site	Phase	WMA/MSWD-F (ka)	± 1σ	n/N	MSWD/N-1
Onano Upper Sillar						
N316.MS1	LAT35-s	Sanidine (TF)	207.0	0.9	7/27	1.06
N320.MS1	LAT35-l	Leucite (TF)	206.9	0.7	6/9	1.11
N324.MS1	LAT35	Leucite (SH)	220.1	1.9	10/10	0.44
N317.MS1	LAT40-s	Sanidine (TF)	210.7	0.7	14/27	1.21
N322.MS1	LAT40-l	Leucite (TF)	215.1	0.7	7/7	1.94
N325.MS1	LAT40	Leucite (SH)	215.7	1.8	13/13	3.09
N.319.MS1	LAT41-s	Sanidine (TF)	212.5	0.9	5/25	1.26
N321.MS1	LAT41-l	Leucite (TF)	208.8	1.0	8/8	0.87
N323.MS1	LAT41	Leucite (SH)	205.9	1.0	9/11	1.09
Onano Spatter						
N412-482.MS3	LAT07	Sanidine (TF)	216.3	0.9	33/54	1.33
N291.MS1	LAT07-d	Sanidine (TF)	209.9	2.0	27/27	1.00
N420.MS3	LAT07	Leucite #1 (SH)	233.1	3.5	28/28	1.52
N422.MS3	LAT07	Leucite #2 (SH)	241.8	5.3	28/28	0.89
N425.MS3	LAT07	Leucite #3(SH)	241.1	5.9	14/14	0.71
N416-426.MS3	LAT38	Sanidine (TF)	219.3	0.6	40/54	1.33
N292.MS1	LAT38-d	Sanidine (TF)	221.4	2.2	21/22	0.96
Onano Lower Sillar						
N417-427.MS3	LAT39	Sanidine (TF)	214.1	1.1	16/54	1.36
Grotte di Castro						
N418-419.MS3	LAT06	Sanidine (TF)	213.2	1.1	23/54	1.37
N413.MS3	LAT10	Sanidine (TF)	213.2	0.9	20/27	1.47
N415.MS3	LAT37	Sanidine (TF)	214.7	1.1	15/27	1.59
N421.MS3	LAT37	Leucite #1 (SH)	225.3	3.1	28/28	0.61
N423.MS3	LAT37	Leucite #2 (SH)	217.2	3.2	14/14	0.51
N424.MS3	LAT37	Leucite #3(SH)	236.9	3.6	13/13	0.27
N411.MS3	LAT04	Sanidine (TF)	211.0	0.9	18/26	1.15

Note. (TF), single-grain total fusion; (SH), single grain step-heating; (-s), sanidine; (-l), leucite; (-d), duplicate run on another mass-spectrometer. (MWA), weighted mean age (by SH); (MSWD-F), MSWD-filtered juvenile component (by TF). n/N, number of crystal (TF) or step (SH) included in the WMA/MSWD-F estimate over total number of measurements, N. (MSWD/N-1), normalized figure of merit (CHI-2 score).

Figure 7d). These juvenile estimates would make Onano Upper Sillar resolvably younger than Grotte di Castro Fm. (by 2.70 ± 0.64 kyr at the 95% confidence level) assuming that the MSWD-F provides an unbiased estimator of the depositional age. This is, however, not the case judging from the other data. The pooled MSWD-F estimate of Onano Lower Sillar (214.1 ± 1.1 ka, Figure 7c) would make this unit coeval with Grotte di Castro Fm. but younger than Onano Spatter Fm. (MSWD-F = 218.0 ± 0.5 ka, Figure 7a), which is prohibited by stratigraphic relationships as the Onano Lower Sillar underlies the Onano Spatter Fm. We infer that such a discrepancy reflects a bias inherent to the MSWD-F estimate which blindly pools the youngest sanidine ages to derive a juvenile (depositional) age for each individual site. This is particularly evident in the case of Onano Spatter Fm. The sites from this unit return widely scattered MSWD-F estimates between 209 and 219 ka (Figure 10 and Table 2) for samples supposed to belong to the same eruptive event or phase. The between-site juvenile-mode scatter is over ∼10 kyr, far beyond statistical uncertainties involved in the MSWD-F calculations. Note that this cannot be due to insufficient statistics since the data coverage is sufficiently extensive to produce a continuous distribution for each sample.

Table 3
Spread Parameters Used in Common Juvenile Model Calculations

Run#	Site	Phase	Spread (kyr)	±1σ	Max Age (ka)	±1σ	Min age (ka)	±1σ	ρ
Onano Upper Sillar									
N316.MS1	LAT35-s	Sanidine (TF)	45.5	3.8	245.2	1.8	199.7	3.4	0.47
N320.MS1	LAT35-l	Leucite (TF)	11.9	1.4	217.6	0.9	205.7	1.0	0.66
N317.MS1	LAT40-s	Sanidine (TF)	54.8	5.0	260.7	1.9	205.9	4.6	0.38
N322.MS1	LAT40-l	Leucite (TF)	13.3	5.1	218.9	1.7	205.6	4.8	0.33
N319.MS1	LAT41-s	Sanidine (TF)	44.2	4.9	251.3	4.0	207.1	2.8	0.82
N321.MS1	LAT41-l	Leucite (TF)	11.0	5.8	213.7	2.6	202.7	5.2	0.45
Onano Spatter									
N412-4828.MS3	LAT07	Sanidine (TF)	70.8	14.1	273.8	9.6	203.0	10.3	0.68
N291.MS1	LAT07-d	Sanidine (TF)	46.2	21.4	236.3	13.2	190.1	16.9	0.62
N416-426.MS3	LAT38	Sanidine (TF)	54.1	9.6	264.1	5.4	210.0	8.0	0.56
N292.MS1	LAT38-d	Sanidine (TF)	36.7	14.6	237.3	10.8	200.6	9.9	0.74
Onano Lower Sillar									
N417-427.MS3	LAT39	Sanidine (TF)	67.2	9.7	273.0	9.0	205.8	3.8	0.92
Grotte di Castro									
N418-419.MS3	LAT06	Sanidine (TF)	96.6	15.8	282.3	8.7	185.7	13.3	0.55
N413.MS3	LAT10	Sanidine (TF)	57.6	14.4	252.3	8.0	194.7	12.0	0.56
N415.MS3	LAT37	Sanidine (TF)	74.7	24.1	274.1	20.9	199.4	12.1	0.86
N411.MS3	LAT04	Sanidine (TF)	26.0	18.0	230.7	11.1	204.7	14.2	0.62

Note. (Spread, kyr), empirical differences between maximum (Max age, ka) and minimum (Min age, ka) age of continuous distribution (i.e., with extreme outliers trimmed out). Data used are those marked in bold in Table S2 of Supporting Information S1. (ρ), error correlation coefficient between Spread and Max age parameters.

This situation is different for Grotte di Castro samples. These behave more coherently despite exhibiting as much internal scatter yet with mutually consistent MSWD-F juvenile estimates (Figure 10 and Table 2). We trace this distinct behavior to the distinct texture and petrography of Onano Spatter Fm. compared to the other units. The former is dominated by scoriae and abundant lithic material characteristic of coarse proximal deposits that are absent in the more homogenous distal facies making up the bulk of the other deposits (Sections 2 and 3.3). This suggests sanidine contamination of the spatter samples (LAT07 and LAT38) by massive incorporation and reworking of pre-eruptive material (e.g., from subvolcanic syenite levels and apophyses), a mechanism more heavily affecting this facies than the other units. Hand-picked sanidines from the Onano spatter deposits appeared free of inclusions and euhedral, although in thin section (Figure 4) broken fragments of sanidine crystals surrounded by glass are common. The case for selective excess contamination is another option (than xeno/antecrystic contamination) to explain the age spread but is not supported by the leucite and sanidine data which record the same trend/spread despite these two minerals being structurally known to differently accommodate excess Ar (Wartho et al., 2005). Also, isochron calculations do not indicate any systematic contamination with non-atmospheric trapped argon (Figure S3 in Supporting Information S1). As already noted by Landi and D'Oriano (2020), these older ages may represent antecrysts from an older crystal mush located on the upper wall of the reservoir and remobilized during the eruption. Sanidine crystals may also have been incorporated from syenite apophyses representing slowly-cooled equivalents of trachytic to trachyphonolitic melts of older Latera subvolcanic products during caldera collapse.

Textural evidence from Best and Christiansen (1997) shows that broken sanidine phenocrysts can take on shapes similar to newly formed crystals, preserving the elongated shape or breaking along the 010 or 001 faces. This, along with the 5% HF-treatment applied to remove adhering glass, may have hampered recognition of such broken crystals during separation, and many of them may have been included in the separate. Evidence for a shallow syenitic intrusion is provided by deep geothermal boreholes (Barberi et al., 1984; Bertrami et al., 1984; Nappi et al., 1991) in the central sector of the Latera caldera. Such bodies may represent a former, pre-eruptive

crystal-rich reservoir or melt potentially remobilized during the spatter eruption. Accordingly, we interpret the older and sectorially variable age of the scoria sanidines to result from massive incorporation (or wholesale remobilization) of antecrysts from one (or several) older crystal mush(es) near the apex of the upper wall of the reservoir (see Landi & D'Oriano, 2020, and discussion further below).

A striking feature of all samples, including the spatter facies, is that their ordered age spectra overlap each one another almost perfectly when grouped by unit (Figure 11). Things appear as if all units were loaded with broadly the same sanidine cargo (in terms of age componentry, at the scale of the unit), but with internal variations in mixture proportions (at the scale of the sample) distinctly controlled by extraction dynamics from a zoned or compound magma chamber or from older (pre-eruptive) shallow magmatic bodies. In Figure 10 the individual (within-sample) age distributions are all seen to emanate from a common baseline age near 205 ka (shown with maximum-likelihood horizontal error bars as determined below), irrespective of the spread internally covered. The latter is reflected by variable MSWD-F estimates in the companion spectrum plot (Figure 10), chiefly as a result of internal variations in proportion of "juvenile" crystals in a given sample. It is worth to note that all samples display one (or more) ages consistent with the baseline age at 205 ka, strongly suggesting the possibility of a shared juvenile component across all dated units.

We tested such a possibility in a plot Δ_{age} (= internal age spread) versus T_{max} (= oldest recorded component) for each dated sample using the relevant data summarized in Table 3 and computing a MLE for a common juvenile component (Figure 12). In such a plot, the $^{40}Ar/^{39}Ar$ ages should indeed align along a 1:1 slope projecting to a common zero-spread age if the samples share the same juvenile component. The data are indeed seen to project within error to a common juvenile component at 205.3 ± 1.4 ka (±1σ MLE, MSWD/N-1 = 0.69). Note that this trend is deemed particularly robust in the case of the Onano Upper Sillar that includes independent sanidine + leucite sample pairs consistent with a common juvenile component as assumed by the model (see further below). All other samples are also consistent with this estimate, including those from Onano Spatter, Onano Lower Sillar, and Grotte di Castro, all intersecting the trend within error (Figure 12).

We emphasize that our MLE juvenile estimate is not equivalent to simply pooling the youngest ages of the different units. Standard pooling schemes as summarized elsewhere (e.g., Schaen et al., 2020) do not include a built-in test for a shared juvenile end-member among different samples from the same suite. As a result, they cannot return an independent test of mutual concordance otherwise than by pooling each MSWD-F estimate altogether, with the risk of quadratically averaging (i.e., reducing) the error of the final pooled estimate. This is unlike our dedicated MLE model that carries over the test over the different units taken together while returning the appropriate MLE error accordingly (which is indeed ± 1.3 ka, i.e., greater than would be returned by MSWD-F pooling at ± 0.8 ka). More importantly, the MLE model is based on explicit rules to combine the observables objectively, making no assumption on specific pre-eruptive ages or survival time to derive the juvenile component. This contrasts with model-dependent Bayesian strategies assuming pre-eruption age distributions ("survivorship closure function") to infer the residence time and most probable eruption age for a single depositional unit (Mucek et al., 2021; Van Zalinge et al., 2022).

We also emphasize that collinearity in the MLE plot does not necessarily imply contemporaneity since Sorano Fm. would plot in the middle of the trend as well. The MLE estimate is specifically intended as a ground-test model for statistically estimating a shared juvenile endmember under the assumption that the dated samples are coeval. Contemporaneity in our case is independently confirmed by the congruent paleomagnetic directions shared by Onano and Grotte di Castro Fms. regionally (see Section 4.1). Taken together, the paleomagnetic data and the best-fitting juvenile mode thus corroborate the model that these units were indeed emplaced shortly, if not instantly, that is, within less than one or two centuries around 205 ka. In the present circumstances, the MLE strategy circumvents the limitations inherent to the standard MSWD-F estimate in identifying a common juvenile component from the pooled suite (compare with Figure 10, upper plot). These findings provide compelling evidence that Grotte di Castro and Onano Fms. do not represent separate eruptions as previously considered, but likely belong to a single, large-scale caldera-forming event that we suggest merging and rename as "Grotte di Castro-Onano" climactic eruption.

5.2. The Leucite Record

Independent evidence that $^{40}Ar/^{39}Ar$ age variations occur in connection with a sectorially-controlled pre-eruptive chamber structure is also provided by the leucite data. Fresh (un-analcimized) leucite crystals dated along with

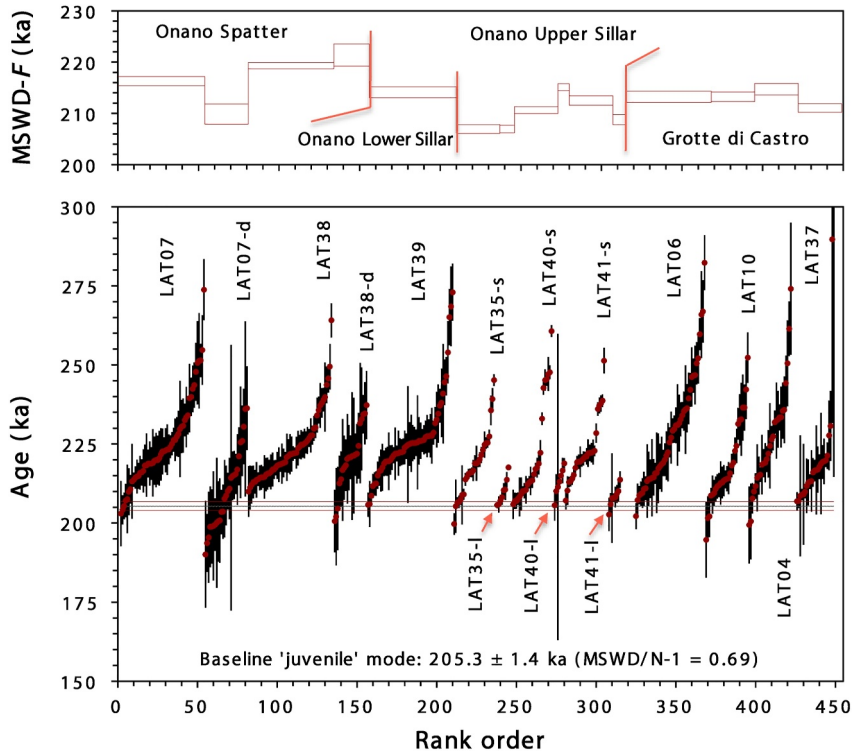

Figure 10. Compound $^{40}Ar/^{39}Ar$ single-grain age distribution in all dated units. Upper plot: MSWD-filtered juvenile component (MSWD-F, ± 1σ) for each sampled site (or sample) with unit provenance indicated. Lateral extent of each error box in the spectrum refers to the corresponding rank interval in the plot underneath (with sample name indicated). Lower plot: age-ordered distribution of individual total-fusion ages for each individual sampled site. Baseline "juvenile" mode as calculated in text and plotted at ± 1σ. N, number of measurements. Note the characteristic age spread recorded over 50 kyr in all samples from their common juvenile baseline at 205 ka. (-s), sanidine; (-l), leucite; (-d), duplicate run on another mass-spectrometer.

sanidine in both Grotte di Castro and Onano Fms. display variations between 205 and 241 ka, a range very similar to the age spread of sanidine whatever the unit or sample considered (Figure 10 and Tables 2 and 3). Leucite crystals extracted from the matrix of Onano (samples LAT35, LAT40, LAT41) yielded ages varying between 206 ± 1 ka and 220 ± 2 ka (Table 2) while those from the spatter facies are characteristically older, in the range 220–240 ka (LAT07, see Table 3). This nicely parallels the trend of older ages already noted for sanidine in this unit and, very importantly, occurs in the same age range as the companion sanidine, strongly suggesting they bear the same geologic significance. Interestingly, the Grotte di Castro Fm. also display leucite ages as old as 240 ka (LAT37, see Table 2), in parallel with the tail of old sanidine ages also found in this unit (Figure 7a).

Along with the lack of evidence for wholesale contamination with non-atmospheric trapped argon (see isochron data in Figure S3 of Supporting Information S1), such a parallelism argues against contamination by excess Ar to explain the old leucite ages and favors a common origin by contamination with antecrysts and/or xenocrysts as previously recognized by Nappi et al. (1991, 1995), Turbeville (1993) and Landi and D'Oriano (2020) at Latera. In particular, Landi and D'Oriano (2020) observed that leucite crystals from phonotephritic samples of Onano Spatter may belong to the phonolitic crystal mush/melt scavenged by the phonotephrite melt during eruption. This is supported by experimental data excluding leucite and phlogopite as stable liquidus phases in a phonotephritic melt (Conte et al., 2009; Pichavant et al., 2014). Contamination by pre-eruptive $^{40}Ar/^{39}Ar$ leucite ages is already known from similar pyroclastic deposits elsewhere (e.g., Roccamonfina volcano, Italy; Scaillet et al., 2008). Importantly, all step-heating analyses conducted on leucite here show flat plateau-like patterns (Figure 8), indicating closed-system behavior since their first closure. Further, existing diffusion data for leucite (Wartho et al., 2005) indicate that this mineral is much faster Ar-diffusing than K-feldspar which is estimated to be completely degassed in a matter of years to centuries at 700–750°C (for a 1 mm radius grain; Spell et al., 2001; Andersen et al., 2017). This excludes preservation of pre-eruptive leucite ages for even moderate residence times

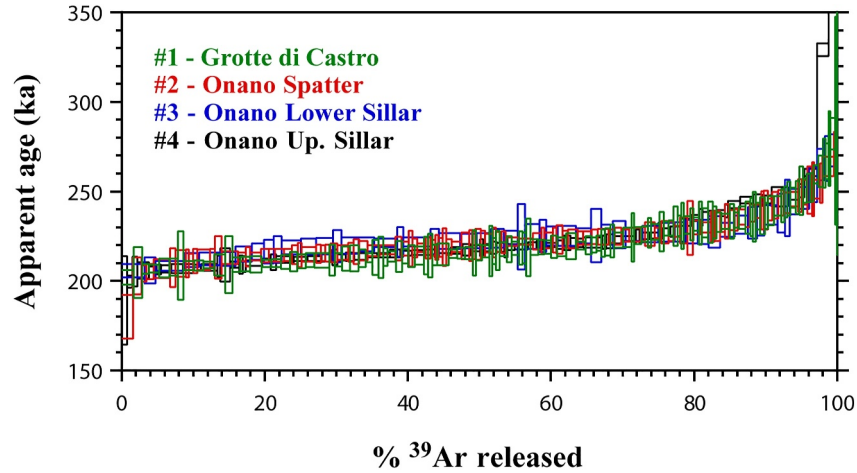

Figure 11. Age-ordered spectra of Grotte di Castro and Onano units. Note almost perfect overlap of the age distribution among all units.

(i.e., centuries) at magmatic temperatures. This strongly argues in favor of their remobilization as antecrysts or xenocrysts from near-wall cold storage, as already suggested for sanidine in similar contexts (Andersen et al., 2017; Cooper, 2019; Mucek et al., 2021; Stelten et al., 2018; Van Zalinge et al., 2022).

Note that the older leucite step-heating ages are characteristically defined by the biggest crystals best suited for such experiments. Optically (in thin section, Figure 5d), these may display a peritectic destabilization reaction (leucite + liquid = K-feldspar rim) and are clearly identified as antecrysts, consistent with petrographic and textural evidence of remobilization of sanidine + leucite crystals from syenitic subvolcanic bodies and leucite-bearing intrusives (Nappi et al., 1991), or antecryst inherited from a phonolitic melts/crystal mush (Landi & D'Oriano, 2020). In contrast, the smaller-sized leucite grains analyzed by total-fusion (Onano Upper Sillar Fm., Table 2) record the youngest ages found near 205 ka (Figure 10). These are too small (and often analcimized) or absent in thin section to properly characterize their origin as inherited (antecryst, xenocryst) juvenile or late-crystallized crystals in equilibrium with the last melt. We note however that these young leucite ages fundamentally agree with the baseline juvenile age collectively defined near 205 ka by the sanidine + leucite ensemble (Figure 10). This strongly supports this age as marking the terminal magmatic activity (and eruption) of the system.

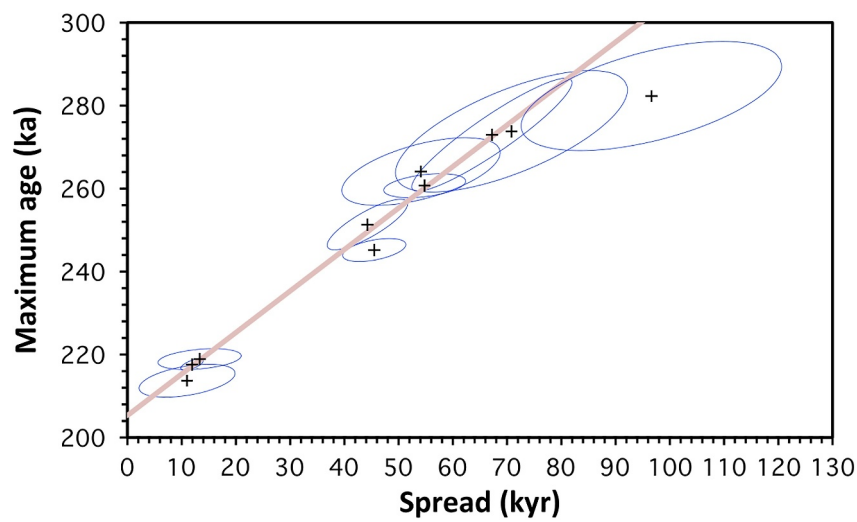

Figure 12. Common juvenile component plot defined as the Maximum-Likelihood Estimate line with slope 1:1 intersecting the 65.5% C.I. ellipses of the corresponding data in Table 3. Best-fit juvenile age is defined by the intercept with the vertical axis.

Figure 13. (a) Synthetic depositional sequence representative of the intermediate/distal deposits of the Grotte di Castro-Onano eruption. Not to scale. (b) Location of the sites studied for each deposit. DEM model is derived from Tarquini et al. (2007).

As emphasized by previous detailed petrographic studies, most crystals in the Onano deposits represent either cumulate crystals at the walls of the magma reservoir(s) or foreign crystals associated with less evolved melts (Landi & D'Oriano, 2020). We infer that the older leucite ages are meaningful in terms of long-term pre-eruptive cold storage near the apical or wall-rock portions of the pre-caldera magma chamber, supporting a model of sectorial extraction from a pre-existing mush (Landi & D'Oriano, 2020) and/or remobilization by fragmentation of subvolcanic precursors (Nappi et al., 1991) during the climactic Grotte di Castro-Onano eruption. Pre-eruptive crystals (antecrysts) were most likely segregated in crystal-locked mushes at the top of the magmatic system, at storage-T low enough (450 to < 600°C; Andersen et al., 2017) to retain $^{40}Ar^*$ produced by in situ decay, until remobilization by the Grotte di Castro-Onano eruption. The similarity in age distribution between sanidine and leucite further suggests that a cold margin of the magma chamber developed over the lifetime of magma chamber build-up and maturation, a process that may have lasted at least for ~40–50 kyr based on the age spread recorded by all units (Figure 11).

5.3. Reconstruction of the Grotte di Castro-Onano Eruption Dynamics

Integration of the Grotte di Castro and Onano units into a single eruptive sequence changes the perspective on eruption dynamics controlling the final stages of caldera evolution at Latera. A conceptual model integrating our data with field observations and previous work is sketched in Figure 13, where a composite depositional sequence comprising the intermediate/distal deposits of Grotte di Castro Fm. (SW of the caldera) and the proximal/intermediate facies of Onano Fm. (NE of the caldera) is displayed. Based on this synthetic record, we reconstruct below the dynamics of caldera formation as it can be inferred from time-space variations in (a) local depositional facies, (b) melt extraction dynamics, and (c) sectorial interactions with the local caldera (and reservoir) structure.

Our emphasis is on placing scattered (and so far, poorly interrelated) field observations in a coherent perspective of caldera formation dynamics.

After the eruption of Sorano Fm. (220.1 ± 1.1 ka), the Latera caldera experienced a long-lasting volcanic quiescence during which the Sorano ignimbrite was deeply dissected and a ubiquitous, 0.5 m-thick soil bed formed. The volcanic reactivation of the caldera was heralded by the sudden rise of mafic magma that reached the surface producing an explosive eruption. The occurrence of this event is testified by the presence, E-SE of the LVC, of a fine-grained, black, coarse-ash-sized, fallout layer with plane-parallel stratification overlying a paleosol (Figure 2b–13; Colucci et al., 2013; Vezzoli et al., 1987). This primary black ash layer is separated from the overlying deposits only by a thin reworked ash bed with no evidence of weathering, indicative of a short time-lapse between the events (Figure 13). This suggests that part of the magma feeding the mafic eruption eventually stalled at, and potentially destabilized, the base of a pre-existing felsic reservoir underneath the caldera, likely triggering the Grotte di Castro-Onano caldera-forming eruption.

The onset of the Grotte di Castro-Onano eruption initiated with the formation of a sustained, convective column producing an inversely graded pumice lapilli fallout south and east of the LVC. The progressive rise of the sustained, fully convective eruptive column was followed by a regime dominated by column unsteadiness. This evolution is recorded by the presence, SE of the LVC, of matrix-rich, cross-bedded beds (PDC deposits; Figure 13) intercalated with finer grained, clast-supported lapilli beds indicating fallout from short-lived, transient and lowered convective columns. The fallout appears to have a fairly large cross-wind dispersal as indicated by correlative beds in the eastern and northern sectors (LAT42 and LAT39; Figure 13), supporting a W-NW- to E-SE-directed dispersal.

About 6 km SE of the caldera center, the fallout layers are replaced by 1–3 m-thick, matrix-supported, poorly sorted ash and lapilli beds with plane-parallel to low-angle cross-bedding (Figure 13). Structural and lithological features of the basal, dune-bedded, ash-rich deposits are variable to the N and W of the caldera (Pitigliano sector) compared to the south. The westward propagation of the early PDCs is also characterized by the presence, in the basal ash-rich tuff-bed, of abundant radially oriented (parallel to flow direction) tree holes formerly forming a dense forest at the moment of the eruption. The western basal ash-rich tuff bed might represent the distal-lateral equivalent of the early surges or more likely of the lower sillar unit E of the LVC.

The first evidence of caldera collapse is marked in the eruptive sequence by the emplacement of the Lower Lithic-rich, coarse Breccia unit deposited in the NE of the caldera (Figure 13; Landi & D'Oriano, 2020; Palladino & Simei, 2005) and is associated upwards with a spatter agglomerate unit and a spatter-rich pyroclastic flow emplaced to the N-NE of the LVC (Spatter Unit; Figure 13). Macro- and micro-scale features of the breccia and spatter deposit previously attributed to Onano are suggestive of a transient eruption phase characterized by intense brecciation of the rock pile overlying the magma chamber via the activation of ring faults. This phase was characterized by the forceful ejection, possibly from multiple vents, of breccia along with moderately fragmented magma (scoriae) incorporating a substantial amount of non-juvenile material (lithics and crystals). As the eruption progressed toward a phase of further widening and deepening of the caldera structure, the Upper Lithic-rich Breccia was deposited (Figure 14). Features of these deposits fit well the massive to stratified breccia lithofacies (mlBr) and massive agglomerate lithofacies (mAg) of Branney and Kokelaar (2002), characteristic of large caldera-forming eruptions. Differences in magma discharge rate and spatter versus pumice ejecta at different vents likely resulted in lateral/sectorial variations in eruptive style as suggested for the Campanian Ignimbrite eruption (Campi Flegrei, Italy; Rosi et al., 1996). The presence of a carbonate structural high striking NNW-SSE in the central-eastern part of the present-day Latera caldera (Barberi et al., 1984), might have influenced the vents opening and the localization of the caldera collapse, similar to the Cape Riva eruption (Santorini, Greece; Druitt, 1985; Heiken & McCoy Jr, 1984), the Siwi pyroclastic sequence (Tanna, Vanuatu; Allen, 2004), and the Sutri eruption (Vico volcano, Italy; Bear et al., 2009a, 2009b). At this stage of the eruption, the entire plumbing system was involved (Landi & D'Oriano, 2020), giving rise to extensive magma mingling.

At intermediate and distal locations, the Lithic-rich Upper Breccia is seen to grade upwards and laterally into diffuse-bedded, strongly lithified, ash and lithic-rich ignimbrite, showing the typical hardened sillar-color (Figure 13; Upper Sillar). The Upper Sillar ignimbrite is widely distributed all around the caldera and was likely emplaced during the climactic phase of the eruption, when the magma mass discharge and PDCs runout peaked.

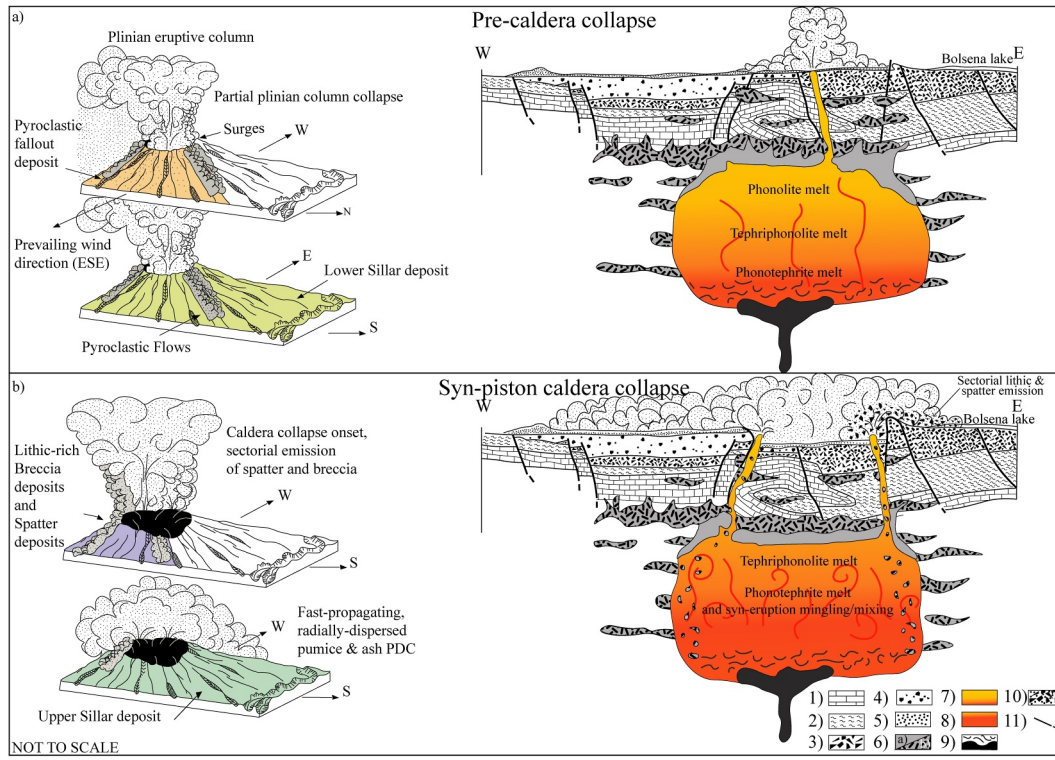

Figure 14. Schematic cartoon illustrating, on the right, the (a) pre-syn eruptive (modified after Bear et al., 2009b) and (b) syn-late eruptive magma reservoir and, on the left, the relative mechanisms, depositional features and the whole phenomena of the Grotte di Castro-Onano caldera-forming eruption (modified after Landi & D'Oriano, 2020). Geological section is modified after Barberi et al. (1984) and Nappi et al. (1991). (1) Tuscan Nappe: limestones, marls and cherty limestones (also thermally metamorphosed); (2) Ligurian Flysch: marls and calcareous sandstones; (3) pre-Latera ignimbrite leucite bearing lava flows (LVC) and/or leucite-bearing lava flows and pyroclastics of the Bolsena and Paleobolsena volcanic complexes; (4) volcanic breccias of the pre-Grotte di Castro-Onano ignimbrites; (5) pyroclastics (pre-Grotte di Castro Onano Formation) of the LVC products; (6) syenitic to leucite bearing rocks and crystal mushes, as evidenced by ENEL-UNG exploratory drillcores L1, L3, L5, and L10 (Barberi et al., 1984; Bertrami et al., 1984; Nappi et al., 1991) and here interpreted as deriving from (a) the subvolcanic crystallization of the Grotte di Castro-Onano magma batches (cognates) and (b) magmatic cold storage, including shallow-level material emplaced before the Grotte di Castro-Onano caldera-forming eruption and/or pre caldera activity; (7) Main magma batch (tephriphonolite to phonolite) of the Grotte di Castro-Onano Formation; (8) Late spilling of magma due to the piston collapse of the Grotte di Castro-Onano caldera-forming eruption (tephriphonolite to phonotephrite); (9) arrival of more primitive magma remobilizing reservoir and crystal mushes and triggering the Grotte di Castro-Onano eruption (black ash fallout precursor); (10) Spatter and Lithic-rich Breccia deposits; (11) faults.

The proposed reconstruction provides a coherent explanation for a number of features such as: (a) the radial distribution of a single (rather than multiple) ignimbrite sheet all around the caldera, as expected for a high-intensity PDC; (b) the inferred high magnitude of the event, consistent with the formation of a caldera of the size of Latera (about 10 km across); and (c) the occurrence of sectorially-controlled lithic-rich facies indicating foundering by caldera collapse(s) with emission vents locally controlled by the northern rim of the caldera (the spatter and breccia deposits previously attributed to Onano).

In this scheme, the 205 ka age of the Grotte di Castro-Onano eruptive event marks the paroxysmal and closing stage of the caldera formation. The Grotte di Castro-Onano pyroclastic sequence is either overlain by reworked material or cut by an erosional surface at different sites (e.g., LAT16 and LAT30; Figure 13), and is locally unconformably capped by the "Tufi di Poggio Pinzo" tephra sequence in the NW of the LVC (Landi & D'Oriano, 2020). The stratigraphically younger Tufi di Poggio Pinzo and Pitigliano Formation is loosely dated by K/Ar between 185 ± 4 ka and 166 ± 4 ka (Pitigliano Formation, Metzeltin & Vezzoli, 1983), and at 158 ± 7 ka by $^{40}Ar/^{39}Ar$ (Turbeville, 1992; Table S1 in Supporting Information S1). It is correlated with the Vepe caldera structure, a younger and very local collapse of the nested Latera caldera system (Figure 1; Nappi & Renzulli, 1990). This event accounts for only a very local modification of the finite structure of the Latera caldera

which was largely shaped by the Grotte di Castro-Onano eruptive unit. Our revised chronology reduces the time span of caldera development to a few tens of thousands years (50–60 ky) relative to previous estimates (120 ka; Brocchini et al., 2000; Marra, Bahain, et al., 2019; Marra, Costantini et al., 2019; Monaco et al., 2022; Metzeltin & Vezzoli, 1983; Nappi et al., 1991, 1995; Turbeville, 1992).

5.4. Cold-Storage $^{40}Ar/^{39}Ar$ Systematics: Implications for the Plumbing System and Timescales of Magma Reactivation

The preservation of pre-eruptive, cold-storage, sanidine $^{40}Ar/^{39}Ar$ ages has been reported for a growing number of large-scale caldera systems worldwide (Andersen et al., 2017; Mucek et al., 2021; Van Zalinge et al., 2022). Such a process has been successfully modeled in terms of reactive melt flow caused by buoyant melt percolating and reacting upwards through a stratified mushy reservoir, producing low-crystallinity and chemically differentiated magmas rising up through the column (Annen et al., 2006; Cooper & Kent, 2014; Jackson et al., 2018; Karakas et al., 2017; Peressini et al., 2007; Rubin et al., 2017; Rudnick, 1995; Sisson et al., 2005; Solano et al., 2014). In these models, changes in local composition and pre-eruptive thermal history can rapidly increase melt fractions, leading to the remobilization of early formed crystals kept in cold storage for most of the time-life and incubation time of the system, explaining the incorporation and preservation of older (pre-eruptive) crystal ages in younger (juvenile) melt fractions.

A similar, layered, pre-eruptive chemical configuration has been suggested for the LVC by Landi and D'Oriano (2020), summarized in Figure 14, with an intermediate tephriphonolitic melt grading upward into a phonolitic crystal mush developed atop of the chamber, with episodic upward migration of evolved interstitial melts derived from closed-system crystal fractionation of tephriphonolite and forming lenses of evolved phonolite at the top of the eruptible reservoir (Figure 14a). Melt-solid equilibria through the column indicates that all K-feldspar phenocrysts formed in equilibrium with the (apical) phonolitic melts and represent fragments of a crystal mush located near the upper wall of the reservoir (Figure 14). Similarly, leucite phenocrysts now found in the phonotephritic samples are inferred to result from the mechanical admixing of phonolitic melts/crystal mush into the hybrid phonotephritic intermediates during eruption (Landi & D'Oriano, 2020; Figure 14b).

According to Landi and D'Oriano (2020), phase-equilibrium modeling indicates that the intermediate tephriphonolite melt was produced later by convective (i.e., mechanical) mixing between the phonotephrite and phonolite end-members, rather than by incremental crystal fractionation of phonolite from phonotephrite in the pre-eruptive magma reservoir (Figure 14a). The systematic preservation of pre-eruptive ages in all units (Figure 11) excludes a scenario of whole-scale convection in favor of a coherent reservoir column maintaining a thermally and compositionally stable layered structure until fast and wholesale remobilization during magma withdrawal. In this scenario, convection must have been initially restricted to pods and discrete km-thick layers (sills/laccolith), precluding through-going (vertical) inter-mixing with the crystal-locked (sanidine ± leucite) apical phonolite mush. As suggested by Landi and D'Oriano (2020), the feeding and maturation process of the pre-eruptive column likely occurred by incremental growth via successive injections and accretion of discrete, high-level, phonolitic layers/sills, potentially on timescales ~40–50 kyr (or longer) as indicated by the pre-eruptive timespan recorded by sanidine and leucite (Figure 11). Mechanical destabilization and reactivation across the whole column leading to syn-eruptive mingling-mixing of the different pre-eruptive magmas (Landi & D'Oriano, 2020; Figure 14b) must have suddenly followed, on timescales short enough to avoid protracted communication with (and reheating of) the upper mush layer and permitting the partial preservation of pre-eruptive ages throughout the depositional sequence.

On textural and petrographic grounds, Landi and D'Oriano (2020) suggested the presence of broken sanidine crystals in Onano Fm. to result from the mechanical disaggregation during forceful magma ascent through the crystal mush lining the roof of the magma chamber. From the $^{40}Ar/^{39}Ar$ perspective and on account of the pervasive contamination of all depositional facies by pre-eruptive ages (Figure 11), this mechanism is suggested to have affected the majority of products (re)mobilized throughout the caldera (including pre-collapse deposits), reinforcing the view of catastrophic failure and remobilization of the pre-eruptive column during piston-collapse of the caldera system (Figure 14b).

The parallelism between the petrologic and Ar isotopic record is striking and shows that destabilization operated in concert with sectorial magma extraction (rather than by wholesale disruption of the column/chamber zoning), in such a way to preserve local differences in storage conditions and sanidine ± leucite cargo. As noted earlier, the

MSWD-F juvenile estimates vary with depositional facies across the eruptive sequence (Figure 10). The phonotephritic scoriae are the juvenile component which by far contain the highest amount of broken sanidine crystals accompanied by leucite xenocrysts, implying remobilization of colder (or already cooled) material carrying pre-eruptive ages (Figure 14b). The older $^{40}Ar/^{39}Ar$ ages are also those closely associated with spatter agglomerates rich in explosively reworked, near-wall country-rock material remobilized during the phase of ring faults activation and roof collapse in the middle of the sequence (Figure 13) NE of the caldera, indicating that caldera failure was likely driven by the pre-eruptive roof structure there.

A major implication of this model and the supporting $^{40}Ar/^{39}Ar$ evidence (i.e., the continuous age distribution in Figure 11) is that the bulk of the sanidine (±leucite) cargo must originate from the upper mushy layers, with only a minor fraction contributed by the underlying levels, in agreement with the petrologic record (Landi & D'Oriano, 2020). Should the model be correct, the Latera case shows that reliance of individual MSWD-based estimates from scattered locations is highly likely to miss the tiny but relevant information contained in the data. Complex, sector-driven $^{40}Ar/^{39}Ar$ systematics such as described here are likely to be common to other young, highly-evolved caldera systems equally affected by selective remobilization of a vertically and thermally stratified reservoir. This work shows that coupling paleomagnetism with fine-scale petrology and regionally extensive $^{40}Ar/^{39}Ar$ dating is mandatory in such cases for successfully resolving individual caldera-forming events at the millennial scale.

6. Conclusions

Based on an integrated approach combining paleomagnetism with single-grain $^{40}Ar/^{39}Ar$ dating and field depositional analysis, our study of the Latera caldera system leads to the following main results.

1. Two major depositional units previously identified as two separate eruptive events (Grotte di Castro and Onano Formations) are shown to represent a single, major, "Grotte di Castro-Onano" caldera-forming event; this is supported by independent and consistent paleomagnetic directions and a common emplacement age near 205 ka identified both on sanidine and leucite juvenile crystals from proximal and distal facies.
2. Within-unit and caldera-wide single-grain $^{40}Ar/^{39}Ar$ age variations >50 kyr are found to occur in connection with lateral and stratigraphic depositional facies variations; these are argued to reflect pre-eruptive ages remobilized from cold storage. The crystal cargo and petrography suggest sectorially-controlled melt extraction from distinct levels in the vertical/zonal structure of the pre-eruptive reservoir by piston-collapse; the preservation of broadly similar pre-eruptive age variations across the different depositional facies, either distal or proximal, suggests vigorous melt + crystal remobilization during terminal collapse and foundering.
3. Along with the $^{40}Ar/^{39}Ar$ record, the physical volcanology of the Grotte di Castro-Onano event indicates that it was one of the largest-volume and highest-intensity event of the Latera Volcanic Complex. The eruption started with a high-intensity Plinian eruption gradually evolving from locally distributed PDC's into widely dispersed ignimbrite sheets when piston-collapse occurred and the mass discharge peaked. By analogy with other lag-breccias and spatter agglomerates recognized worldwide (Santorini, Campanian Ignimbrite, Siwi ignimbrite-Vanuatu, Sutri eruption), the spatter agglomerate formerly identified as the Coarse Breccia unit of Onano Formation (NE of the caldera) can now be framed into a regionally and temporally coherent scenario of sectorially-controlled depositional dynamics during the climactic Grotte di Castro-Onano piston-collapse event.

One of the most relevant aspects of this study is the recognition of a continuum in $^{40}Ar/^{39}Ar$ age distribution between cognate + juvenile crystals in each depositional unit of Grotte di Castro-Onano. This finding suggests the presence of a vertically arrayed pre-eruptive reservoir capped by a mushy zone likely consisting of a network of accreted phonolitic layers assembled during protracted (about 40–50 kyr) maturation of the magmatic system and representing the cold-storage source of pre-eruptive crystals remobilized during the climactic 205 ka caldera-forming Grotte di Castro-Onano event. We speculate that syn-eruptive remobilization of older crystals as seen at Latera is symptomatic of vigorous magma remobilization and withdrawal, with implosion of the chamber walls due to pressure drop, seismic shaking, and mechanical failure of the magma chamber roof during piston collapse. Catastrophic remobilization of pre-eruptive crystals during large-scale, piston-collapse eruptions is likely to be common to other caldera systems elsewhere (Andersen et al., 2017; Van Zalinge et al., 2022).

Conflict of Interest

The authors declare no conflicts of interest relevant to this study.

Data Availability Statement

Paleomagnetic and $^{40}Ar/^{39}Ar$ data used for supporting this study are available at Malaguti et al. (2024) with free access. Remasoft 3.0 was used as paleomagnetic data browser and analyzer (written Chadima, 2006). Software used to make figures include Adobe Illustrator (© 2022 Adobe), QGIS (QGIS.org, %%Y. QGIS Geographic Information System. QGIS Association. http://www.qgis.org, version 3.36.3), Microsoft Excel 365 (© Microsoft), PaleomagPlot (unpublished, written by Pignatelli Alessandro and Francesca D'Ajello Caracciolo, INGV). $^{40}Ar/^{39}Ar$ computations made and plotted with in-house software according to procedures published and described in full in Scaillet (2000, DOI: 10.1016/S0009-2541(99)00149-7). The PmagPy function "watson_v," was used for paleomagnetic analysis, developed by Tauxe et al. (2016) (for the code https://pmagpy.github.io/PmagPy-docs/documentation_notebooks/PmagPy_plots_analysis.html#watsons-v).

Acknowledgments

This work is part of the ABM PhD project. The authors particularly thank A. Todrani, M.S. Voloschina, S. Costa, A. Magli and R. Malaguti for their help in the fieldwork. We thank F. Duval for help and support during the Ar/Ar analysis at the Ar/Ar laboratory of the Institut des Sciences de la Terre d'Orléan (CNRS-Orléans). L. Vezzoli, D. Palladino, P. Landi and C. D'Oriano are acknowledged for helpful discussions. The owners of the Pozzolana Montenero s.a.s. and Cantoniera quarry are deeply thanked for having allowed our sampling in their quarries. We are grateful to three referees (Shanaka de Silva, Mark Stelten, and an anonymous reviewer), to *JGR Solid Earth* Associate Editor, and to Editor Mark Dekkers for providing constructive comments that helped to improve the work considerably. Work supported by LABEX grant VOLTAIRE (ANR-10-LABX-100-01), the Région Centre grant ARGON, and the EQUIPEX grant PLANEX (ANR-11-EQPX-0036). Open access publishing facilitated by Istituto Nazionale di Geofisica e Vulcanologia, as part of the Wiley - CRUI-CARE agreement.

References

Acocella, V. (2021). *Volcano-tectonic processes*. Springer International Publishing. https://doi.org/10.1007/978-3-030-65968-4

Allen, S. R. (2004). Complex spatter-and pumice-rich pyroclastic deposits from an andesitic caldera-forming eruption: The Siwi pyroclastic sequence, Tanna, Vanuatu. *Bulletin of Volcanology*, *67*(1), 27–41. https://doi.org/10.1007/s00445-004-0358-6

Andersen, N. L., Jicha, B. R., Singer, B. S., & Hildreth, W. (2017). Incremental heating of Bishop Tuff sanidine reveals preeruptive radiogenic Ar and rapid remobilization from cold storage. *Proceedings of the National Academy of Sciences* (Vol. 114(47), pp. 12407–12412). https://doi.org/10.1073/pnas.1709581114

Annen, C., Blundy, J. D., & Sparks, R. S. J. (2006). The genesis of intermediate and silicic magmas in deep crustal hot zones. *Journal of Petrology*, *47*(3), 505–539. https://doi.org/10.1093/petrology/egi084

Baag, C., Helsley, C. E., Xu, S. Z., & Lienert, B. R. (1995). Deflection of paleomagnetic directions due to magnetization of the underlying terrain. *Journal of Geophysical Research*, *100*(B6), 10013–10027. https://doi.org/10.1029/95jb00148

Barberi, F., Innocenti, F., Landi, P., Rossi, U., Saitta, M., Santacroce, R., & Villa, I. M. (1984). The evolution of Latera caldera (central Italy) in the light of subsurface data. *Bulletin of Volcanology*, *47*(1), 125–141. https://doi.org/10.1007/BF01960544

Bear, A. N., Cas, R. A. F., & Giordano, G. (2009a). The implications of spatter, pumice and lithic clast rich proximal co-ignimbrite lag breccias on the dynamics of caldera forming eruptions: The 151 ka Sutri eruption, Vico volcano, Central Italy. *Journal of Volcanology and Geothermal Research*, *181*(1–2), 1–24. https://doi.org/10.1016/j.jvolgeores.2008.11.032

Bear, A. N., Cas, R. A. F., & Giordano, G. (2009b). Variations in eruptive style and depositional processes associated with explosive, phonolitic composition, caldera-forming eruptions: The 151 ka Sutri eruption, Vico caldera, central Italy. *Journal of Volcanology and Geothermal Research*, *184*(3–4), 225–255. https://doi.org/10.1016/j.jvolgeores.2009.04.005

Bertrami, R., Cameli, G. M., Lovari, F., & Rossi, U. (1984). Discovery of Latera geothermal field: Problems of the exploration and Research. In *U. N. Economic commission for europe, seminar on utilization of geothermal energy for electric power production and space heating, firenze, 14–17 may, 1984*.

Best, M. G., & Christiansen, E. H. (1997). Origin of broken phenocrysts in ash-flow tuffs. *The Geological Society of America Bulletin*, *109*(1), 63–73. https://doi.org/10.1130/0016-7606(1997)109<0063:oobpia>2.3.co;2

Best, M. G., Christiansen, E. H., Deino, A. L., Grommé, C. S., & Tingey, D. G. (1995). Correlation and emplacement of a large, zoned, discontinuously exposed ash flow sheet: The $^{40}Ar/^{39}Ar$ chronology, paleomagnetism, and petrology of the Pahranagat Formation, Nevada. *Journal of Geophysical Research*, *100*(B12), 24593–24609. https://doi.org/10.1029/95jb01690

Bogue, S. W., & Coe, R. S. (1981). Paleomagnetic correlation of Columbia River basalt flows using secular variation. *Journal of Geophysical Research*, *86*(B12), 1883–1897. https://doi.org/10.1029/JB086iB12p11883

Branca, S., D'Ajello Caracciolo, F., Malaguti, A. B., & Speranza, F. (2019). Constraining age and volume of lava flow invasions of the Alcantara valley, Etna volcano (Italy). New insights from paleomagnetic dating and 3D magnetic modeling. *Journal of Volcanology and Geothermal Research*, *374*, 13–25. https://doi.org/10.1016/j.jvolgeores.2019.02.009

Branney, M., & Acocella, V. (2015). *Calderas. The encyclopedia of volcanoes* (pp. 299–315). Elsevier.

Branney, M. J., & Kokelaar, P. (1992). A reappraisal of ignimbrite emplacement: Progressive aggradation and changes from particulate to non-particulate flow during emplacement of high-grade ignimbrite. *Bulletin of Volcanology*, *54*(6), 504–520. https://doi.org/10.1007/bf00301396

Branney, M. J., & Kokelaar, P. (2002). *Pyroclastic density currents and the sedimentation of ignimbrites*. (Vol. 27, p. 142). Geological Society.

Brocchini, D., Di Battistini, G., Laurenzi, M. A., Vernia, L., & Bargossi, G. M. (2000). New $^{40}Ar/^{39}Ar$ datings on the southeastern sector of the Vulsinian volcanic district (central Italy). *Bollettino della Societa Geologica Italiana*, *119*, 113–120.

Butler, R. F. (2004). *Paleomagnetism: Magnetic domains to geological terranes*. Blackwell Scientific Publications.

Chadima, M. (2006). Remasoft 3.0 a user-friendly paleomagnetic data browser and analyzer. *Travaux Géophysiques*, *27*, 20.

Cole, J. W., Milner, D. M., & Spinks, K. D. (2005). Calderas and caldera structures: A review. *Earth-Science Reviews*, *69*(1–2), 1–26. https://doi.org/10.1016/j.earscirev.2004.06.004

Colucci, S., Palladino, D. M., Mulukutla, G. K., & Proussevitch, A. A. (2013). 3-D reconstruction of ash vesicularity: Insights into the origin of ash-rich explosive eruptions. *Journal of Volcanology and Geothermal Research*, *255*, 98–107. https://doi.org/10.1016/j.jvolgeores.2013.02.002

Conte, A. M., Dolfi, D., Gaeta, M., Misiti, V., Mollo, S., & Perinelli, C. (2009). Experimental constraints on evolution of leucite-basanite magma at 1 and 10-4 GPa: Implications for parental compositions of roman high-potassium magmas. *European Journal of Mineralogy*, *21*(4), 763–782. https://doi.org/10.1127/0935-1221/2009/0021-1934

Conticelli, S., Francalanci, L., Manetti, P., & Peccerillo, A. (1987). Evolution of Latera volcano, Vulsinian district (Central Italy): Stratigraphical and petrological data. *Periodico di Mineralogia*, *56*(2–3), 175–199.

Cooper, K., & Kent, A. (2014). Rapid remobilization of magmatic crystals kept in cold storage. *Nature*, *506*(7489), 480–483. https://doi.org/10.1038/nature12991

Cooper, K. M. (2019). Time scales and temperatures of crystal storage in magma reservoirs: Implications for magma reservoir dynamics. *Philosophical Transactions of the Royal Society A*, *377*(2139), 20180009. https://doi.org/10.1098/rsta.2018.0009

Corti, G., Cioni, R., Franceschini, Z., Sani, F., Scaillet, S., Molin, P., et al. (2019). Aborted propagation of the Ethiopian rift caused by linkage with the Kenyan rift. *Nature Communications*, *10*(1), 1309. https://doi.org/10.1038/s41467-019-09335-2

Druitt, T. H. (1985). Vent evolution and lag breccia formation during the Cape Riva eruption of Santorini, Greece. *The Journal of Geology*, *93*(4), 439–454. https://doi.org/10.1086/628965

Druitt, T. H., Calder, E. S., Cole, P. D., Hoblitt, R. P., & Loughlins, S., Norton, G. E., et al. (2002). *Small-volume, highly mobile pyroclastic flows formed by rapid sedimentation from pyroclastic surges at Soufrière Hills volcano, Montserrat: An important volcanic hazard*. Geological Society, London, Memoirs, (Vol. 21(21), pp. 263–279). https://doi.org/10.1144/gsl.mem.2002.021.01.12

Fisher, R. A. (1953). Dispersion on a sphere. *Proceedings of the Royal Society of London, Series A* (Vol. 217(1130), pp. 295–305). https://doi.org/10.1098/rspa.1953.0064

Fisher, R. V. (1990). Transport and deposition of a pyroclastic surge across an area of high relief: The 18 may 1980 eruption of Mount St. Helens, Washington. *The Geological Society of America Bulletin*, *102*(8), 1038–1054. https://doi.org/10.1130/0016-7606(1990)102<1038:tadoap>2.3.co;2

Franceschini, Z., Cioni, R., Scaillet, S., Corti, G., Sani, F., Isola, I., et al. (2020). Recent volcano-tectonic activity of the Ririba rift and the evolution of rifting in South Ethiopia. *Journal of Volcanology and Geothermal Research*, *403*, 106989. https://doi.org/10.1016/j.jvolgeores.2020.106989

Gansecki, C. A., Mahood, G. A., & McWilliams, M. O. (1996). $^{40}Ar/^{39}Ar$ geochronology of rhyolites erupted following collapse of the Yellowstone caldera, Yellowstone plateau volcanic field: Implications for crustal contamination. *Earth and Planetary Science Letters*, *142*(1–2), 91–107. https://doi.org/10.1016/0012-821x(96)00088-x

Griffiths, R. W. (2000). The dynamics of lava flows. *Annual Review of Fluid Mechanics*, *32*(1), 477–518. https://doi.org/10.1146/annurev.fluid.32.1.477

Grommé, C. S., McKee, E. H., & Jr Blake, M. C. (1972). Paleomagnetic correlations and potassium argon dating of middle Tertiary ash flow sheets in the eastern Great Basin, Nevada and Utah. *The Geological Society of America Bulletin*, *83*(6), 1619–1638. https://doi.org/10.1130/0016-7606(1972)83[1619:PCAPDO]2.0.CO;2

Heiken, G., & McCoy Jr, F. (1984). Caldera development during the Minoan eruption, Thira, Cyclades, Greece. *Journal of Geophysical Research*, *89*(B10), 8441–8462. https://doi.org/10.1029/jb089ib10p08441

Hildreth, W., & Mahood, G. (1985). Correlation of ash-flow tuffs. *The Geological Society of America Bulletin*, *96*(7), 968–974. https://doi.org/10.1130/0016-7606(1985)96<968:coat>2.0.co;2

Jackson, M. D., Blundy, J., & Sparks, R. S. J. (2018). Chemical differentiation, cold storage and remobilization of magma in the Earth's crust. *Nature*, *564*(7736), 405–409. https://doi.org/10.1038/s41586-018-0746-2

Karakas, O., Degruyter, W., Bachmann, O., & Dufek, J. (2017). Lifetime and size of shallow magma bodies controlled by crustal-scale magmatism. *Nature Geoscience*, *10*(6), 446–450. https://doi.org/10.1038/ngeo2959

Kirschvink, J. L. (1980). The least-square line and plane and the analysis of paleomagnetic data. *Geophysical Journal of the Royal Astronomical Society*, *62*(3), 699–718. https://doi.org/10.1111/j.1365-246x.1980.tb02601.x

Korte, M., Brown, M. C., Gunnarson, S. R., Nilsson, A., Panovska, S., Wardinski, I., & Constable, C. G. (2019). Refining Holocene geochronologies using palaeomagnetic records. *Quaternary Geochronology*, *50*, 47–74. https://doi.org/10.1016/j.quageo.2018.11.004

Landi, P., & D'Oriano, C. (2020). The Onano eruption (Latera volcano, Central Italy): An example of magma mixing/mingling as dominant process in a caldera-forming eruption. *Contributions to Mineralogy and Petrology*, *175*(9), 1–24. https://doi.org/10.1007/s00410-020-01724-x

Lanza, R., & Meloni, A. (2006). *The Earth's magnetic field* (pp. 1–66). Springer Berlin Heidelberg.

Lanza, R., & Zanella, E. (2006). *Comments on "Chronology of Vesuvius' activity from AD 79 to 1631 based on archeomagnetism of lavas and historical sources"*. In C. Principe, et al. (Eds.) (Vol. 68(4). pp. 394–396). Bulletin of Volcanology. https://doi.org/10.1007/s00445-005-0030-9

Lipman, P. W. (1997). Subsidence of ash-flow calderas: Relation to caldera size and magma-chamber geometry. *Bulletin of Volcanology*, *59*(3), 198–218. https://doi.org/10.1007/s004450050186

Magli, A., Branca, S., Speranza, F., Risica, G., Siravo, G., & Giordano, G. (2021). Paleomagnetic dating of prehistoric lava flows from the urban district of Catania (Etna volcano, Italy). *Bulletin*, *134*(3–4), 616–628. https://doi.org/10.1130/b36026.1

Magli, A., Speranza, F., Branca, S., Corsaro, R. A., Coltelli, M., Malaguti, A. B., & Giordano, G. (2024). Testing paleomagnetic dating on prehistoric flank eruptions from SE slope of Etna Volcano. *Journal of Geophysical Research: Solid Earth*, *129*(9), e2023JB028314. https://doi.org/10.1029/2023jb028314

Malaguti, A. B., Branca, S., Speranza, F., Coltelli, M., Del Carlo, P., & Renzulli, A. (2023). Age of the Valle del Bove formation and chronology of the post-collapse flank eruptions, Etna volcano (Italy). *Journal of Volcanology and Geothermal Research*, *434*, 107752. https://doi.org/10.1016/j.jvolgeores.2023.107752

Malaguti, A. B., Rosi, M., Pistolesi, M., Speranza, F., & Menzies, M. (2022). The contribution of palaeomagnetism, tephrochronology and radiocarbon dating to refine the last 1100 years of eruptive activity at Vulcano (Italy). *Bulletin of Volcanology*, *84*(1), 1–19. https://doi.org/10.1007/s00445-021-01515-7

Malaguti, A. B., Scaillet, S., Pistolesi, M., Rosi, M., Speranza, F., & Renzulli, A. (2024). Coupled paleomagnetism and $^{40}Ar/^{39}Ar$ dating of Latera ignimbrites (Vulsini Volcanic District, Italy) unravel processes associated to piston-collapse calderas [Dataset]. *Zenodo*. https://doi.org/10.5281/zenodo.14266130

Marra, F., Bahain, J. J., Jicha, B., Nomade, S., Palladino, D. M., Pereira, A., et al. (2019). Reconstruction of the MIS 5.5, 5.3 and 5.1 coastal terraces in Latium (central Italy): A re-evaluation of the sea-level history in the Mediterranean Sea during the last interglacial. *Quaternary International*, *525*, 54–77. https://doi.org/10.1016/j.quaint.2019.09.001

Marra, F., Costantini, L., Di Buduo, G. M., Florindo, F., Jicha, B., Monaco, L., et al. (2019). Combined glacio-eustatic forcing and volcano-tectonic uplift: Geomorphological and geochronological constraints on the Tiber river terraces in the eastern Vulsini volcanic district (central Italy. *Global and Planetary Change*, *182*, 103009. https://doi.org/10.1016/j.gloplacha.2019.103009

Marsella, M., Palladino, D. M., & Trigila, R. (1987). The Onano pyroclastic formation (Vulsini volcanoes): Depositional features, distribution and eruptive mechanisms. *Periodico di Mineralogia*, *56*, 223–238.

McDougall, I., & Harrison, T. M. (1999). *Geochronology and Thermochronology by the $^{40}Ar/^{39}Ar$ method*. Oxford University Press.

Metzeltin, S., & Vezzoli, L. (1983). Contributi alla geologia del Vulcano di Latera (Monti Vulsini, Toscana meridionale-Lazio settentrionale). *Memorie della Società Geologico Italiana*, *25*, 247–271.

Monaco, L., Leicher, N., Palladino, D. M., Arienzo, I., Marra, F., Petrelli, M., et al. (2022). The Fucino 250–170 ka tephra record: New insights on peri-Tyrrhenian explosive volcanism, central Mediterranean tephrochronology, and timing of the MIS 8-6 climate variability. *Quaternary Science Reviews*, *296*, 107797. https://doi.org/10.1016/j.quascirev.2022.107797

Moore, I., & Kokelaar, P. (1998). Tectonically controlled piecemeal caldera collapse: A case study of Glencoe volcano, Scotland. *The Geological Society of America Bulletin*, *110*(11), 1448–1466.

Mucek, A. E., Danišík, M., de Silva, S. L., Miggins, D. P., Schmitt, A. K., Pratomo, I., et al. (2021). Resurgence initiation and subsolidus eruption of cold carapace of warm magma at Toba Caldera, Sumatra. *Communications Earth and Environment*, *2*(1), 185. https://doi.org/10.1038/s43247-021-00260-1

Nappi, G. (1969a). Genesi ed evoluzione della Caldera di Latera. *Bollettino del Servizio Geologica d'Italia*, *90*, 61–68.

Nappi, G. (1969b). Stratigrafia e petrografia dei Vulsini occidentali (Caldera di Latera). Nota preliminare. *Bollettino della Società geologica italiana*, *40*, 171–181.

Nappi, G., & Renzulli, A. (1990). Genesi ed evoluzione della caldera del Vepe. *Memorie Descrittive Carta Geologica d'Italia*, *38*, 129–144.

Nappi, G., Renzulli, A., & Santi, P. (1991). Evidence of incremental growth in the Vulsinian calderas (central Italy). *Journal of Volcanology and Geothermal Research*, *47*(1–2), 13–31. https://doi.org/10.1016/0377-0273(91)90098-K

Nappi, G., Renzulli, A., Santi, P., & Gillot, Y. P. (1995). Geological evolution and geochronology of the Vulsini volcanic district (central Italy). *Bollettino della Societa Geologica Italiana*, *114*, 599–613.

Niespolo, E. M., Rutte, D., Deino, A. L., & Renne, P. R. (2017). Intercalibration and age of the Alder Creek sanidine 40Ar/39Ar standard. *Quaternary Geochronology*, *39*, 205–213. https://doi.org/10.1016/j.quageo.2016.09.004

Ort, M. H., de Silva, S. L., Jiménez, N. C., Jicha, B. R., & Singer, B. S. (2013). Correlation of ignimbrites using characteristic remanent magnetization and anisotropy of magnetic susceptibility, central Andes, Bolivia. *Geochemistry, Geophysics, Geosystems*, *14*(1), 141–157. https://doi.org/10.1029/2012GC004276

Ort, M. H., Rosi, M., & Anderson, C. D. (1999). Correlation of deposits and vent locations of the proximal Campanian Ignimbrite deposits, Campi Flegrei, Italy, based on natural remanent magnetization and anisotropy of magnetic susceptibility characteristics. *Journal of Volcanology and Geothermal Research*, *91*(2–4), 167–178. https://doi.org/10.1016/S0377-0273(99)00034-7

Palladino, D. M., & Simei, S. (2005). Eruptive dynamics and caldera collapse during the Onano eruption, Vulsini, Italy. *Bulletin of Volcanology*, *67*(5), 423–440. https://doi.org/10.1007/s00445-004-0385-3

Palladino, D. M., Simei, S., Sottili, G., & Trigila, R. (2010). Integrated approach for the reconstruction of stratigraphy and geology of quaternary volcanic terrains: An application to the Vulsini volcanoes (central Italy). In G. E. Groppelli & L. Viereck (Eds.), *Stratigraphy and geology in volcanic areas* (Vol. 464, pp. 66–84). Geological Society of America.

Palladino, D. M., Simei, S., & Triglia, R. (2016). *Note Illustrative della Carta geologica d'Italia alla scala 1:50.000, foglio 344 Tuscania*. ISPRA-Servizio Geologico d'Italia (In Italian). Retrieved from https://www.isprambiente.gov.it/Media/carg/note_illustrative/344_Tuscania.pdf

Pavón-Carrasco, F. J., Osete, M. L., Torta, J. M., & De Santis, A. (2014). A geomagnetic field model for the Holocene based on archaeomagnetic and lava flow data. *Earth and Planetary Science Letters*, *388*, 98–109. https://doi.org/10.1016/j.epsl.2013.11.046

Pavón-Carrasco, F. J., Osete, M. L., Torta, J. M., & Gaya-Piqué, L. R. (2009). A regional archeomagnetic model for Europe for the last 3000 years, SCHA. DIF. 3K: Applications to archeomagnetic dating. *Geochemistry, Geophysics, Geosystems*, *10*(3). https://doi.org/10.1029/2008GC002244

Peressini, G., Quick, J. E., Sinigoi, S., Hofmann, A. W., & Fanning, M. (2007). Duration of a large mafic intrusion and heat transfer in the lower crust: A SHRIMP U-Pb zircon study in the Ivrea-Verbano zone (western Alps, Italy). *Journal of Petrology*, *48*(6), 1185–1218. https://doi.org/10.1093/petrology/egm014

Phillips, D., Matchan, E. L., Gleadow, A. J., H. Brown, F., A. McDougall, I., Cerling, T. E., et al. (2023). 40Ar/39Ar eruption ages of Turkana basin tuffs: Millennial-scale resolution constrains palaeoclimate proxy tuning models and hominin fossil ages. *Journal of the Geological Society*, *180*(4), jgs2022–jgs2171. https://doi.org/10.1144/jgs2022-171

Phillips, D., Matchan, E. L., Honda, M., & Kuiper, K. F. (2017). Astronomical calibration of $^{40}Ar/^{39}Ar$ reference minerals using high-precision, multi-collector (ARGUSVI) mass spectrometry. *Geochimica et Cosmochimica Acta*, *196*, 351–369. https://doi.org/10.1016/j.gca.2016.09.027

Pichavant, M., Scaillet, B., Pommier, A., Iacono-Marziano, G., & Cioni, R. (2014). Nature and evolution of primitive Vesuvius magmas: An experimental study. *Journal of Petrology*, *55*(11), 2281–2310. https://doi.org/10.1093/petrology/egu057

Pistolesi, M., Isaia, R., Marianelli, P., Bertagnini, A., Fourmentraux, C., Albert, P. G., et al. (2016). Simultaneous eruptions from multiple vents at Campi Flegrei (Italy) highlight new eruption processes at calderas. *Geology*, *44*(6), 487–490. https://doi.org/10.1130/g37870.1

Pistolesi, M., Rosi, M., Malaguti, A. B., Lucchi, F., Tranne, C. A., Speranza, F., et al. (2021). Chronostratigraphy of the youngest (last 1500 years) rhyolitic eruptions of Lipari (Aeolian Islands, Southern Italy) and implications for distal tephra correlations. *Journal of Volcanology and Geothermal Research Res*, *420*, 107397. https://doi.org/10.1016/j.jvolgeores.2021.107397

Risica, G., Speranza, F., Giordano, G., De Astis, G., & Lucchi, F. (2019). Palaeomagnetic dating of the Neostromboli succession. *Journal of Volcanology and Geothermal Research*, *371*, 229–244. https://doi.org/10.1016/j.jvolgeores.2018.12.009

Rivera, T. A., Schmitz, M. D., Jicha, B. R., & Crowley, J. L. (2016). Zircon petrochronology and 40Ar/39Ar sanidine dates for the Mesa Falls Tuff: Crystal-scale records of magmatic evolution and the short lifespan of a large Yellowstone magma chamber. *Journal of Petrology*, *57*(9), 1677–1704.

Rosi, M., Vezzoli, L., Aleotti, P., & De Censi, M. (1996). Interaction between caldera collapse and eruptive dynamics during the Campanian Ignimbrite eruption, Phlegraean Fields, Italy. *Bulletin of Volcanology*, *57*(7), 541–554. https://doi.org/10.1007/s004450050111

Rotolo, S. G., Scaillet, S., Speranza, F., White, J. C., Williams, R., & Jordan, N. J. (2021). Volcanological evolution of Pantelleria Island (strait of Sicily) peralkaline volcano: A review. Comptes Rendus. *Geoscience*, *353*(S2), 111–132. https://doi.org/10.5802/crgeos.51

Rubin, A. E., Cooper, K. M., Till, C. B., Kent, A. J., Costa, F., Bose, M., et al. (2017). Rapid cooling and cold storage in a silicic magma reservoir recorded in individual crystals. *Science*, *356*(6343), 1154–1156. https://doi.org/10.1126/science.aam8720

Rudnick, R. L. (1995). Making continental crust. *Nature*, *378*(6557), 571–578. https://doi.org/10.1038/378571a0

Scaillet, S. (2000). Numerical error analysis in $^{40}Ar/^{39}Ar$ dating. *Chemical Geology*, *162*(3–4), 269–298. https://doi.org/10.1016/s0009-2541(99)00149-7

Scaillet, S., & Guillou, H. (2004). A critical evaluation of young (near-zero) K–Ar ages. *Earth and Planetary Science Letters*, *220*(3–4), 265–275. https://doi.org/10.1016/s0012-821x(04)00069-x

Scaillet, S., Rotolo, S. G., La Felice, S., & Vita-Scaillet, G. (2011). High-resolution 40Ar/39Ar chronostratigraphy of the post-caldera (<20 ka) volcanic activity at Pantelleria, Sicily Strait. *Earth and Planetary Science Letters*, *309*(3–4), 280–290. https://doi.org/10.1016/j.epsl.2011.07.009

Scaillet, S., Vita-Scaillet, G., & Guillou, H. (2008). Oldest human footprints dated by Ar/Ar. *Earth and Planetary Science Letters*, *275*(3–4), 320–325. https://doi.org/10.1016/j.epsl.2008.08.026

Scaillet, S., Vita-Scaillet, G., & Rotolo, S. G. (2013). Millennial-scale phase relationships between ice-core and Mediterranean marine records: Insights from high-precision 40Ar/39Ar dating of the green tuff of Pantelleria, Sicily strait. *Quaternary Science Reviews*, *78*, 141–154. https://doi.org/10.1016/j.quascirev.2013.08.008

Schaen, A. J., Jicha, B. R., Hodges, K. V., Vermeesch, P., Stelten, M. E., Mercer, C. M., et al. (2020). Interpreting and reporting $^{40}Ar/^{39}Ar$ geochronologic data. *GSA Bulletin*, *133*(3–4), 461–487. https://doi.org/10.1130/B35560.1

Sisson, T. W., Ratajeski, K., Hankins, W. B., & Glazner, A. F. (2005). Voluminous granitic magmas from common basaltic sources. *Contributions to Mineralogy and Petrology*, *148*(6), 635–661. https://doi.org/10.1007/s00410-004-0632-9

Solano, J. M. S., Jackson, M. D., Sparks, R. S. J., & Blundy, J. D. (2014). Evolution of major and trace element composition during melt migration through crystalline mush: Implications for chemical differentiation in the crust. *American Journal of Science*, *314*(5), 895–939. https://doi.org/10.2475/05.2014.01

Sparks, R. S. J. (1975). Stratigraphy and geology of the ignimbrites of Vulsini volcano, Italy. *Geologische Rundschau*, *64*(1), 497–523. https://doi.org/10.1007/BF01820680

Spell, T. L., Smith, E. I., Sanford, A., & Zanetti, K. A. (2001). Systematics of xenocrystic contamination: Preservation of discrete feldspar populations at McCullough Pass caldera revealed by 40Ar/39Ar dating. *Earth and Planetary Science Letters*, *190*(3–4), 153–165. https://doi.org/10.1016/s0012-821x(01)00382-x

Speranza, F., Branca, S., Coltelli, M., D'Ajello Carac¬ciolo, F., & Vigliotti, L. (2006). How accurate is "paleomagnetic dating"? New evidence from historical lavas from Mount Etna. *Journal of geophysical Research: Solid Earth*, *111*(B12). https://doi.org/10.1029/2006JB004496

Speranza, F., Di Chiara, A., & Rotolo, S. G. (2012). Correlation of welded ignimbrites on Pantelleria (Strait of Sicily) using paleomagnetism. *Bulletin of Volcanology*, *74*(2), 341–357. https://doi.org/10.1007/s00445-011-0521-9

Steiger, R. H., & Jäger, E. (1977). Subcommission on geochronology: Convention on the use of decay constants in geo-and cosmochronology. *Earth and Planetary Science Letters*, *36*(3), 359–362. https://doi.org/10.1016/0012-821x(77)90060-7

Stelten, M. E., Champion, D. E., & Kuntz, M. A. (2018). The timing and origin of pre-and post-caldera volcanism associated with the Mesa Falls Tuff, Yellowstone Plateau volcanic field. *Journal of Volcanology and Geothermal Research*, *350*, 47–60. https://doi.org/10.1016/j.jvolgeores.2017.12.002

Stelten, M. E., Cooper, K. M., Vazquez, J. A., Calvert, A. T., & Glessner, J. J. (2015). Mechanisms and timescales of generating eruptible rhyolitic magmas at Yellowstone caldera from zircon and sanidine geochronology and geochemistry. *Journal of Petrology*, *56*(8), 1607–1642. https://doi.org/10.1093/petrology/egv047

Tarquini, S., Isola, I., Favalli, M., & Battistini, A. (2007). TINITALY, a digital elevation model of Italy with a 10 m-cell size (Version 1.0) [Dataset]. *Istituto Nazionale di Geofisica e Vulcanologia (INGV)*. https://doi.org/10.13127/TINITALY/1.0

Tauxe, L., Shaar, R., Jonestrask, L., Swanson-Hysell, N. L., Minnett, R., Koppers, A. A. P., et al. (2016). PmagPy: Software package for paleomagnetic data analysis and a bridge to the magnetics information consortium (MagIC) Database. *Geochemistry, Geophysics, Geosystems*, *17*(6), 2450–2463. https://doi.org/10.1002/2016gc006307

Turbeville, B. N. (1992). $^{40}Ar/^{39}Ar$ ages and stratigraphy of the Latera caldera, Italy. *Bulletin of Volcanology*, *55*(1), 110–118. https://doi.org/10.1007/BF00301124

Turbeville, B. N. (1993). Sidewall differentiation in an alkalic magma chamber: Evidence from syenite xenoliths in tuffs of the Latera caldera, Italy. *Geological Magazine*, *130*(4), 453–470. https://doi.org/10.1017/s0016756800020537

Valentine, G., Palladino, D. M., DiemKaye, K., & Fletcher, C. (2019). Lithic-rich and lithic-poor ignimbrites and their basal deposits: Sovana and Sorano formations (Latera caldera, Italy). *Bulletin of Volcanology*, *81*(4), 1–26. https://doi.org/10.1007/s00445-019-1288-7

Valentine, G. A., Wohletz, K. H., & Kieffer, S. W. (1992). Effects of topography on facies and compositional zonation in caldera-related ignimbrites. *The Geological Society of America Bulletin*, *104*(2), 154–165. https://doi.org/10.1130/0016-7606(1992)104<0154:eotofa>2.3.co;2

Van Zalinge, M. E., Mark, D. F., Sparks, R. S. J., Tremblay, M. M., Keller, C. B., Cooper, F. J., & Rust, A. (2022). Timescales for pluton growth, magma-chamber formation and super-eruptions. *Nature*, *608*(7921), 87–92. https://doi.org/10.1038/s41586-022-04921-9

Vezzoli, L., Conticelli, S., Innocenti, F., Landi, P., Manetti, P., Palladino, D. M., & Trigila, R. (1987). Stratigraphy of the Latera volcanic complex: Proposals for a new nomenclature. *Periodico di Mineralogia*, *56*, 89–110.

Walker, G. P. L. (1983). Ignimbrite types and ignimbrite problems. *Journal of Volcanology and Geothermal Research*, *17*(1–4), 65–88. https://doi.org/10.1016/0377-0273(83)90062-8

Wartho, J. A., Kelley, S. P., & Elphick, S. C. (2005). Estimates of Ar diffusion and solubility in leucite and nepheline: Electron microprobe imaging of Ar distribution in a mineral. *American Mineralogist*, *90*(5–6), 954–962. https://doi.org/10.2138/am.2005.1320

Watson, G. (1983). *Statistics on spheres* (Vol. 6, p. 238). The University of Arkansas Lecture Notes in the Mathematical Sciences.

Watson, G. S. (1956). A test for randomness of directions. *Geophysical Supplements to the Monthly Notices of the Royal Astronomical Society*, *7*(4), 160–161. https://doi.org/10.1111/j.1365-246X.1956.tb05561.x

Wendt, I., & Carl, C. (1991). The statistical distribution of the mean squared weighted deviation. *Chemical Geology: Isotope Geoscience section*, *86*(4), 275–285. https://doi.org/10.1016/0168-9622(91)90010-t

Zellmer, G. F. (2021). Gaining acuity on crystal terminology in volcanic rocks. *Bulletin of Volcanology*, *83*(11), 78. https://doi.org/10.1007/s00445-021-01505-9

Zijderveld, J. D. (1967). A. C. demagnetization of rocks: Analysis of results. In D. W. Collinson, K. M. Creer, & S. K. Runcorn (Eds.), *Methods in paleomagnetism, developments in solid Earth geophysics* (Vol. 3, pp. 254–286). Elsevier. https://doi.org/10.1016/B978-1-4832-2894-5.50049-5